Field fluctuations viscoplastic self-consistent crystal plasticity: Applications to predicting texture evolution during deformation and recrystallization of cubic polycrystalline metals

Iftekhar A. Riyad, Marko Knezevic*

Department of Mechanical Engineering, University of New Hampshire, Durham, NH 03824, USA.

Abstract

Recent advances pertaining to modeling of grain fragmentation during deformation and recrystallization of polycrystalline metals using viscoplastic self-consistent (VPSC) polycrystal plasticity are combined into a field fluctuations VPSC (FF-VPSC) model. The model is a higherorder formulation calculating the second moments of lattice rotation rates based on the second moments of stress fields inside grains and resulting intragranular misorientation distributions. The misorientation distributions are used to define a grain fragmentation sub-model for improving predictions of deformation texture evolution and to formulate kinetics sub-models for nucleation as well as to influence the stored energy governing grain growth for the predictions of recrystallization texture evolution. Formation of a copper-like texture in a moderately high stacking fault energy (SFE) Cu and a brass-like texture in low SFE brass during rolling to very large strains are successfully predicted using the model. Remarkably, the model also predicts recrystallization textures from the deformation textures of the two metals after adjusting tradeoffs between transition-bands and grain boundary nucleation mechanisms. Additionally, rolling and recrystallization of an interstitial-free steel, tension and recrystallization of AA5182-O, and recrystallization of an additively manufacturing cobalt-based alloy MarM-509 are simulated to predict texture evolution. Through these case studies involving multiple alloys and thermomechanical processes we show that, in addition to being predictive with good accuracy, the key advantage of the model lies in its versatility. The FF-VPSC model, simulation results, and insights from the results are presented and discussed in this paper.

Keywords: Crystal plasticity; Texture; Grain fragmentation; Recrystallization; FF-VPSC

⁻

^{*} Corresponding author at: Department of Mechanical Engineering, University of New Hampshire, 33 Academic Way, Kingsbury Hall, W119, Durham, NH 03824, USA. Tel.: +1 603 862 5179; fax: +1 603 862 1865. E-mail address: marko.knezevic@unh.edu (M. Knezevic).

1. Introduction

Long-established viscoplastic self-consistent (VPSC) model is widely used for modeling mechanical behavior and texture evolution during plastic deformation of polycrystalline materials [1-4]. Each grain in the VPSC model is considered as an ellipsoidal inclusion embedded in a homogenous effective medium (HEM), which acts as a polycrystal having the mean properties over constituent grains. The HEM properties are calculated using the self-consistent (SC) homogenization scheme relying on the first moments i.e., the mean values of stress and strain per inclusion [5-7]. As the mean-field model, such standard VPSC model provides a favorable balance between computational efficiency and accuracy compared to more computationally expensive and more accurate full-field model formulations [8-11]. However, mean fields are insufficient for accurate modeling after constituent grains develop high intragranular orientation gradients at large strain levels [12-17]. For example, deformation textures at large plastic strains predicted using the mean field models are sharper than measured since intragranular orientation gradients and grain fragmentation are not modeled [18-21]. Accounting for higher order micromechanical fields and underlying intragranular misorientation spreads can substantially improve the predictive characteristics of VPSC [22].

The second-order formulations begun from the works reported in [23, 24] for composites and in [25-27] for polycrystals. In particular, a finite-strain homogenization model for the macroscopic response of viscoplastic polycrystals in which the linearization not only depends on the first moments but also on the second moments of stress field was developed in [27]. The model relied on the fully optimized second-order (FOSO) variational homogenization method in conjunction with self-consistent estimates for the instantaneous response of a linear comparison composite (LCC) with optimally selected properties. These properties of the LCC depended not only from the first but also from the second moments of stress fields. Updating the lattice rotation rate fluctuations of grains based on the higher order statistical information obtained from the second moment of stress produces the accumulation of intragranular misorientations trends with plastic strain, as formulated in [28, 29]. Taking advantages of such intragranular misorientations trends, a grain fragmentation VPSC [30] and a recrystallization model [31] within VPSC both driven by intragranular fluctuations have been developed. In the former model, the grain fragmentations were not in physical space to create new grains but rather in the orientation space. In the latter model, the misorientation spreads as sources of transition bands and grain boundary bulges as recrystallization nuclei were used to formulate nucleation sub-models for modeling recrystallization [32-34]. Nucleated grains grow owing to the difference in stored energy between the given grain and HEM [35]. For completeness, we reflect that other grain fragmentation [36, 37] and recrystallization [35, 38, 39] models not utilizing the micromechanical stress and strain rate field fluctuations but merely average values of grain quantities and HEM have also been presented in the prior literature. The present work combines these recent developments into a field fluctuations VPSC (FF-VPSC) model capable of fragmenting grains in the physical space for modeling thermo-mechanical response and texture evolution of polycrystalline metals.

This paper is concerned with predicting texture evolution during deformation and recrystallization of cubic polycrystalline metals while accounting for the second-order terms of mechanical fields. Given that recrystallization nuclei occur at deformation induced inhomogeneities such as bands of high orientation gradients and thus high stored energy or grain boundary sub-grain bulges into a neighboring grain [40-44], the recrystallization kinetics is highly dependent on the deformed state of the metal. Hence, a recrystallization model must be informed by an appropriate deformation state of the metal, which is input into the recrystallization model. Accuracy of the recrystallization model is driven by the accuracy of the deformation model. Unlike choosing orientations of the nuclei randomly as in many recrystallization models [45-47], the present work attempts to model nucleation based on the deformed state of the metal with underlying intragranular orientation gradients predicted using FF-VPSC.

First, we attempt to predict rolling textures of face-centered cubic (FCC) metals that develop either a copper-type (Cu-type) texture or a brass-type texture as discussed in [48-50]. The former is favored in rolling of high stacking fault energy (SFE) metals, while the latter is favored in rolling of low SFE metals [51-54]. While the former texture development is well understood and successfully simulated using many crystal plasticity models, the latter is elusive [49, 55]. Since the low SFE metals deform by deformation twinning, the formation of brass-like texture was attributed to deformation twinning [56]. However, the volume fraction of deformation twins produced during deformation is not high enough to completely explain the different textures [49, 55]. In general, predicting brass-like textures using mean-field models with deformation twinning was challenging, especially at high rolling reductions [57-61]. A modified Sachs-type model with random stress fluctuations has been proposed for predicting brass-like texture but the success was limited to low strain levels [62]. Similarly, a viscoplastic ϕ model was developed for simulating brass-like textures but again was not successful at high deformation levels [63]. Furthermore, fullfield simulations with strong latent hardening were able to capture some features of the brass-like texture formation in the early stages but not at the larger stages of deformations [64, 65], presumably due to not modeling the grain break-up behavior [66-68]. In summary, predicting brass-like texture and copper-like texture evolution at high rolling reductions using a single meanfield model was not accomplished in the past. We evaluate predictive characteristics of the FF-VPSC model in predicting both copper-type and brass-type textures at very high strain levels. In doing so, we elucidate the role of misorientation spreads developing in these simulations and resulting transition bands and grain fragmentations. We show that tracking the differences in the grain breakup explains the differences in the texture formation in FCC metals, given the proper selection of deformation mechanisms of slip and twinning.

Next, we simulate recrystallization of the rolling Cu-type and brass-type textures to show utility of the FF-VPSC model in simulating texture evolution during recrystallization. A few additional simulation cases are performed to evaluate the effects of strain-path, stored energy, and crystal structure on the predictions using FF-VPSC. To evaluate the effects of strain path, we simulate texture evolution during simple tension (ST) followed by recrystallization of an aluminum alloy (AA) 5182-O. Developed misorientation trends after ST are compared with experimental

measurements. We then simulate texture evolution during partial recrystallization of a cobalt-based alloy, MarM-509 after its additive manufacturing (AM). The alloy was pre-deformed to a sufficient strain level in compression to provide stored energy and misorientation trends for recrystallization kinetics. Finally, we simulate rolling and recrystallization texture evolution of an interstitial-free steel to evaluate the predictive characteristics for a body-centered cubic (BCC) crystal structure. The predictions of the FF-VPSC model are compared against experimental measurements for every simulation case. Good predictions demonstrate that the consideration of intragranular misorientation fluctuations and grain fragmentation is essential to accurately predict texture evolution during deformation and recrystallization. Predicted recrystallization textures can be adjusted using fractions of transition-bands versus grain boundary nucleation mechanisms.

2. Modeling framework

Following a short summary of the standard VPSC formulation [2, 69], the algorithms to calculate lattice rotation rate fluctuations using intragranular stress field fluctuations are reviewed for completeness of the paper [28]. Next, we describe the formulations to calculate intragranular misorientation spreads and grain fragmentation [29]. Finally, a recrystallization model is described to complete the integrated FF-VPSC framework [31].

Our adopted notation is as follows: the inner products between two vectors or tensors are symbolized by "·" (summation over one contracted index), ":" (summation over two contracted indices) and "::" (summation over four contracted indices). The outer product of two tensors is represented by "⊗". The symmetric deviatoric second-rank tensors are represented by five-dimensional vectors and antisymmetric second-rank tensors are represented by three-dimensional dual vectors [2, 70].

2.1 Formulation of standard VPSC

At a single crystal material point \mathbf{x} , deforming by dislocation glide (and twinning as a pseudo slip [71-73]), the viscoplastic strain rate, $\dot{\boldsymbol{\varepsilon}}(\mathbf{x})$, is given as [2]:

$$\dot{\mathbf{\varepsilon}}(\mathbf{x}) = \sum_{S} \dot{\mathbf{\gamma}}^{S}(\mathbf{x}) \mathbf{m}^{S}(\mathbf{x}), \tag{1}$$

where $\mathbf{m}^s(\mathbf{x}) = \frac{1}{2} (\mathbf{b}^s(\mathbf{x}) \otimes \mathbf{n}^s(\mathbf{x}) + \mathbf{n}^s(\mathbf{x}) \otimes \mathbf{b}^s(\mathbf{x}))$ is the symmetric Schmid tensor of the associated slip system s. \mathbf{n}^s and \mathbf{b}^s are slip plane normal and Burgers vector of slip system s. Shear rate on slip system s at a material point \mathbf{x} , $\dot{\gamma}^s(\mathbf{x})$ is given by:

$$\dot{\gamma}^{S}(\mathbf{x}) = \dot{\gamma}_{0} \left(\frac{|\tau^{S}(\mathbf{x})|}{\tau_{S}^{S}(\mathbf{x})} \right)^{n} \operatorname{sign}(\tau^{S}(\mathbf{x})), \tag{2}$$

where $\dot{\gamma}_0$ is the reference shear rate (assumed to be $1s^{-1}$ in all our calculations), $\tau^s(\mathbf{x}) = \mathbf{m}^s(\mathbf{x})$: $\sigma(\mathbf{x})$ is the resolved shear stress on slip system s, n is the inverse of rate sensitivity (taken to be 20), and τ_c^s is the critical resolved shear stress on slip system s. Substituting Eq. (2) in Eq. (1), we get the nonlinear rate sensitive constitutive relationship between strain rate and stress at local level [74, 75]:

$$\dot{\boldsymbol{\varepsilon}}(\mathbf{x}) = \dot{\gamma}_0 \sum_{\mathcal{S}} \left(\frac{|\boldsymbol{\sigma}(\mathbf{x}) : \mathbf{m}^{\mathcal{S}}(\mathbf{x})|}{\tau_{\mathcal{S}}^{\mathcal{S}}(\mathbf{x})} \right)^n \operatorname{sign}(\boldsymbol{\sigma}(\mathbf{x}) : \mathbf{m}^{\mathcal{S}}(\mathbf{x})) \, \mathbf{m}^{\mathcal{S}}(\mathbf{x}). \tag{3}$$

More details pertaining to the kinematics of VPSC can be found in the literature, e.g. [76, 77]. The non-linear relationship of Eq. (2), at the slip system level can be linearized as:

$$\dot{\gamma}^{s}(\mathbf{x}) = \eta^{s(r)} \tau^{s}(\mathbf{x}) + \dot{g}^{0s(r)},\tag{4}$$

where $\eta^{s(r)}$ is the linearized compliance and $\dot{g}^{0s(r)}$ is the back-extrapolated shear rate of slip system s in grain r. The nonlinear constitutive relationship (Eq. (3)) at the grain level can be linearized similarly as:

$$\dot{\boldsymbol{\varepsilon}}(\mathbf{x}) = \mathbf{M}^{(r)}: \ \boldsymbol{\sigma}(\mathbf{x}) + \dot{\boldsymbol{\varepsilon}}^{0(r)},\tag{5}$$

where $\mathbf{M}^{(r)}$ and $\dot{\mathbf{c}}^{0(r)}$ are the linearized compliance and back-extrapolated strain rate respectively for grain r. Based on the linearization scheme, the formulation of the above moduli can be chosen differently. For this paper, we adopt affine linearization scheme [5]. In the affine linearization, the moduli defined above are:

$$\eta^{s(r)} = n \frac{\dot{\gamma}_0}{\tau_c^{s(r)}} \left(\frac{\tau^{s(r)}}{\tau_c^{s(r)}}\right)^{n-1},\tag{6}$$

$$\dot{g}^{0s(r)} = (1 - n)\dot{\gamma}_0 \left(\frac{\tau^{s(r)}}{\tau_c^{s(r)}}\right)^n \operatorname{sign}(\tau^{s(r)}),\tag{7}$$

$$\mathbf{M}^{(r)} = n\dot{\gamma}_0 \sum_{s} \frac{\mathbf{m}^{s(r)} \otimes \mathbf{m}^{s(r)}}{\tau_c^{s(r)}} \left(\frac{\mathbf{m}^{s(r)} \cdot \mathbf{\sigma}^{(r)}}{\tau_c^{s(r)}} \right)^{n-1}, \tag{8}$$

$$\dot{\boldsymbol{\varepsilon}}^{0(r)} = (1 - n)\dot{\gamma}_0 \sum_{s} \left(\frac{\mathbf{m}^{s(r)} : \boldsymbol{\sigma}^{(r)}}{\tau_c^{s(r)}} \right)^n \operatorname{sign}(\mathbf{m}^{s(r)} : \boldsymbol{\sigma}^{(r)}). \tag{9}$$

After performing the standard self-consistent homogenization, we get the linear relationship analogous to Eq. 5 at the effective medium level as:

$$\dot{\mathbf{E}} = \overline{\mathbf{M}} : \mathbf{\Sigma} + \dot{\mathbf{E}}^0, \tag{10}$$

where Σ and $\dot{\mathbf{E}}$ are the macroscopic stress and strain rate; $\overline{\mathbf{M}}$ is the macroscopic viscoplastic compliance and $\dot{\mathbf{E}}^0$ is the back-extrapolated strain rate.

The macroscopic properties are given by the self-consistent equations as:

$$\overline{\mathbf{M}} = \langle \mathbf{M}^{(r)} : \mathbf{B}^{(r)} \rangle : \langle \mathbf{B}^{(r)} \rangle^{-1}, \tag{11}$$

$$\dot{\mathbf{E}}^{0} = \langle \mathbf{M}^{(r)} : \mathbf{b}^{(r)} + \dot{\mathbf{\epsilon}}^{0(r)} \rangle - \langle \mathbf{M}^{(r)} : \mathbf{B}^{(r)} \rangle : \langle \mathbf{B}^{(r)} \rangle^{-1} : \langle \mathbf{b}^{(r)} \rangle, \tag{12}$$

where $\langle \ \rangle$ denotes volume average. $\mathbf{B}^{(r)}$ and $\mathbf{b}^{(r)}$ are the stress localization tensors which are expresses as the functions of microscopic and macroscopic moduli and can be formulated as:

$$\mathbf{B}^{(r)} = \left(\mathbf{M}^{(r)} + \widetilde{\mathbf{M}}\right)^{-1} : \left(\overline{\mathbf{M}} + \widetilde{\mathbf{M}}\right),\tag{13}$$

$$\mathbf{b}^{(r)} = \left(\mathbf{M}^{(r)} + \widetilde{\mathbf{M}}\right)^{-1} : \left(\dot{\mathbf{E}}^{0} - \dot{\mathbf{\epsilon}}^{0(r)}\right). \tag{14}$$

The self-consistent equations are implicit in the macroscopic moduli, $\overline{\mathbf{M}}$ and $\dot{\mathbf{E}}^0$, and are solved numerically by a fix-point method. $\widetilde{\mathbf{M}}$ is the interaction tensor and is given by:

$$\widetilde{\mathbf{M}} = (\mathbf{I} - \mathbf{S})^{-1} : \mathbf{S} : \overline{\mathbf{M}}, \tag{15}$$

where **S** is the symmetric Eshelby tensor and is the solution of the problem of an inclusion embedded in an effective medium [78]. The interaction equation which relates the deviations in strain rate, $\tilde{\mathbf{\epsilon}}^{(r)}$ and in stress, $\tilde{\mathbf{\sigma}}^{(r)}$ in the inclusion with respect to the macroscopic values is given by:

$$\widetilde{\dot{\mathbf{\epsilon}}}^{(r)} = -\widetilde{\mathbf{M}} : \widetilde{\mathbf{\sigma}}^{(r)}, \tag{16}$$

Total lattice rotation rate field at a material point \mathbf{x} for a grain r, in the absence of macroscopic rigid-body rotation is given as:

$$\dot{\mathbf{\omega}}^{(r)}(\mathbf{x}) = \widetilde{\dot{\mathbf{\omega}}}^{(r)} - \dot{\mathbf{\omega}}^p(\mathbf{x}),\tag{17}$$

where $\tilde{\boldsymbol{\omega}}^{(r)} = \boldsymbol{\Pi} : \mathbf{S}^{-1} : \tilde{\boldsymbol{\varepsilon}}^{(r)}$ is the rigid-body rotation rate of the ellipsoidal inclusion to maintain the compatibility with the effective medium and $\boldsymbol{\Pi}$ is the anti-symmetric Eshelby tensor. $\dot{\boldsymbol{\omega}}^p(\mathbf{x})$ is the lattice rotation rate at material point \mathbf{x} for a grain r which can be given by:

$$\dot{\mathbf{\omega}}^p(\mathbf{x}) = \sum_{s} \dot{\gamma}^s(\mathbf{x}) \mathbf{\alpha}^s(\mathbf{x}),\tag{18}$$

where $\alpha^s(\mathbf{x}) = \frac{1}{2} (\mathbf{b}^s(\mathbf{x}) \otimes \mathbf{n}^s(\mathbf{x}) - \mathbf{n}^s(\mathbf{x}) \otimes \mathbf{b}^s(\mathbf{x}))$ is the antisymmetric part of the Schmid tensor of an associated slip system s.

2.2 Fluctuations of stress and lattice rotation rate

The second moment of stress field (average stress fluctuations) in each grain can be calculated after convergence of the self-consistent iterations at a time t [13]. In our formulation, two sources of intragranular stress fluctuations are considered: mean grain properties variation and spatial variation of orientation inside a grain [22, 29, 79]. The orientation at each grain r at any time t is denoted by active rotation quaternion $\overline{\mathbf{q}}^{t(r)}$. The stress at a material point \mathbf{x} , $\sigma^{t}(\mathbf{x})$ is given by:

$$\sigma^{t}(\mathbf{x}) = \sigma^{t(r)} + \delta \sigma^{t(\bar{q})}(\mathbf{x}). \tag{19}$$

where $\sigma^{t(r)}$ the mean stress in a grain r and $\delta \sigma^{t(\bar{q})}(\mathbf{x})$ is a stress fluctuations term caused by spatial variations of mean grain properties. Adding the fluctuations term does not change the mean term. The second moments of stress in each grain r is calculated as [29]:

$$\langle \mathbf{\sigma}^t \otimes \mathbf{\sigma}^t \rangle^{(r)} = \mathbf{\sigma}^{t(r)} \otimes \mathbf{\sigma}^{t(r)} + \langle \delta \mathbf{\sigma}^{t(\bar{q})} \otimes \delta \mathbf{\sigma}^{t(\bar{q})} \rangle^{(r)} = \frac{2}{w^{t(r)}} \frac{\partial \widetilde{U}_T^t}{\partial \mathbf{M}^{t(r)}}, \tag{20}$$

where $w^{t(r)}$ is the volume fraction of the associated grain r. \widetilde{U}_T^t is the effective stress potential given as [28]:

$$\widetilde{U}_T^t = \frac{1}{2} \overline{\mathbf{M}}^t :: (\mathbf{\Sigma}^t \otimes \mathbf{\Sigma}^t) + \dot{\mathbf{E}}^{0t} : \mathbf{\Sigma}^t + \frac{1}{2} \bar{G}^t.$$
(21)

where \bar{G}^t is the energy under zero applied stress and is expressed using:

$$\bar{G}^t = \sum_r w^{t(r)} \dot{\mathbf{\epsilon}}^{0t(r)} : \mathbf{b}^{t(r)}. \tag{22}$$

After substituting Eq. (21), the term $\frac{2}{w^{t(r)}} \frac{\partial \tilde{U}_{T}^{t}}{\partial \mathbf{M}^{t(r)}}$ from Eq. (20) can be expanded as [13]:

$$\frac{2}{w^{t(r)}} \frac{\partial \tilde{U}_{T}^{t}}{\partial \mathbf{M}^{t(r)}} = \frac{1}{w^{t(r)}} \frac{\partial \bar{\mathbf{M}}^{t}}{\partial \mathbf{M}^{t(r)}} :: \left(\mathbf{\Sigma}^{t} \otimes \mathbf{\Sigma}^{t} \right) + \frac{2}{w^{t(r)}} \frac{\partial \dot{\mathbf{E}}^{0t}}{\partial \mathbf{M}^{t(r)}} : \mathbf{\Sigma}^{t} + \frac{1}{w^{t(r)}} \frac{\partial \bar{G}^{t}}{\partial \mathbf{M}^{t(r)}}. \tag{23}$$

Since the properties in Eq. (23) are calculated via the SC process, the spatial arrangement of the grains has no effect on the stress fluctuations. The second moment expression in Eq. (20) statistically describes the fluctuations of average stress in the absence of any intragranular misorientation. While the second moments of stress can be calculated using the far-right term of Eq. (20), the calculation of the second moment of stress fluctuations caused by variation of mean stress, $\langle \delta \sigma^{t(\bar{q})} \otimes \delta \sigma^{t(\bar{q})} \rangle^{(r)}$, need to be evaluated for second moments of spin and misorientation, as will be evident shortly. Details pertaining to the evaluation of the term is discussed in Appendix B. Next, we incorporate the second source of the fluctuations. If a misorientation quaternion filed, $\delta \mathbf{q}^t(\mathbf{x})$ is introduced at time t inside each grain, the orientation, $\mathbf{q}^t(\mathbf{x})$ at any point \mathbf{x} is defined as [80]:

$$\mathbf{q}^{t}(\mathbf{x}) = \delta \mathbf{q}^{t}(\mathbf{x}) \overline{\mathbf{q}}^{t(r)}. \tag{24}$$

Any orientation or misorientation can be expressed by three independent variables. Therefore, we can express the misorientation quaternion, $\delta \mathbf{q}^t(\mathbf{x})$ by its vector part $\delta \mathbf{r}^t(\mathbf{x})$ [80]. An additional fluctuation of stress, $\delta \mathbf{\sigma}^{t(\delta r)}(\mathbf{x})$ at a point \mathbf{x} , caused by the intragranular misorientation field is superimposed on the stress field defined by Eq. (19) as:

$$\mathbf{\sigma}^{t}(\mathbf{x}) = \mathbf{\sigma}^{t(r)} + \delta \mathbf{\sigma}^{t(\bar{q})}(\mathbf{x}) + \delta \mathbf{\sigma}^{t(\delta r)}(\mathbf{x}). \tag{25}$$

Intragranular stress fluctuations due to misorientation, $\delta \sigma^{t(\delta r)}(\mathbf{x})$ are considered to be linearly proportional to misorientation vector and is expressed by stress derivative taken with respect to misorientation vector as:

$$\delta \mathbf{\sigma}^{t(\delta r)}(\mathbf{x}) = \frac{\partial \mathbf{\sigma}}{\partial \delta \mathbf{r}} \Big|_{\mathbf{\sigma}^{(r)}, \overline{\mathbf{g}}^{(r)}}^{t} \delta \mathbf{r}^{t}(\mathbf{x}), \tag{26}$$

where $\frac{\partial \boldsymbol{\sigma}}{\partial \delta \mathbf{r}}\Big|_{\boldsymbol{\sigma}^{(r)},\overline{\mathbf{q}}^{(r)}}^{t}$ is the rate of change of stress due to intragranular misorientation. The calculation of stress fluctuations due to misorientations, $\delta \boldsymbol{\sigma}^{t(\delta r)}(\mathbf{x})$ has no effect on the average grain stress, $\boldsymbol{\sigma}^{t(r)}$ and fluctuations caused by spatial variations of mean properties, $\delta \boldsymbol{\sigma}^{t(\bar{q})}(\mathbf{x})$ because the volume average of misorientation vector is zero inside each grain, i.e., $\langle \delta \mathbf{r}^t \rangle^{(r)} = \mathbf{0}$.

The second moment of stress in grain r, after considering the intragranular misorientations is:

$$\langle \mathbf{\sigma}^{t} \otimes \mathbf{\sigma}^{t} \rangle^{(r)} = \mathbf{\sigma}^{t(r)} \otimes \mathbf{\sigma}^{t(r)} + \langle \delta \mathbf{\sigma}^{t(\bar{q})} \otimes \delta \mathbf{\sigma}^{t(\bar{q})} \rangle^{(r)} + \langle \delta \mathbf{\sigma}^{t(\delta r)} \otimes \delta \mathbf{\sigma}^{t(\delta r)} \rangle^{(r)} + \\
+ \langle \delta \mathbf{\sigma}^{t(\bar{q})} \otimes \delta \mathbf{\sigma}^{t(\delta r)} \rangle^{(r)} + \langle \delta \mathbf{\sigma}^{t(\delta r)} \otimes \delta \mathbf{\sigma}^{t(\bar{q})} \rangle^{(r)}. \tag{27}$$

where $\langle \delta \boldsymbol{\sigma}^{t(\delta r)} \otimes \delta \boldsymbol{\sigma}^{t(\delta r)} \rangle^{(r)} = \frac{\partial \boldsymbol{\sigma}}{\partial \delta r} \Big|_{\boldsymbol{\sigma}^{(r)}, \overline{\mathbf{q}}^{(r)}}^{t} \langle \delta \mathbf{r}^{t} \otimes \delta \mathbf{r}^{t} \rangle^{(r)} \left(\frac{\partial \boldsymbol{\sigma}}{\partial \delta r} \Big|_{\boldsymbol{\sigma}^{(r)}, \overline{\mathbf{q}}^{(r)}}^{t} \right)^{T}$ represents the second moment of stress fluctuations due to intragranular misorientations, while the fourth and fifth terms of right-hand side of Eq. (27) are cross-covariances of two stress fluctuations field: fluctuations of mean grain properties and misorientation fluctuations inside a grain, $\langle \delta \boldsymbol{\sigma}^{t(\bar{q})} \otimes \delta \boldsymbol{\sigma}^{t(\delta r)} \rangle^{(r)} = \langle \delta \boldsymbol{\sigma}^{t(\bar{q})} \otimes \delta \mathbf{r}^{t} \rangle^{(r)} \left(\frac{\partial \boldsymbol{\sigma}}{\partial \delta r} \Big|_{\boldsymbol{\sigma}^{(r)}, \overline{\mathbf{q}}^{(r)}}^{t} \right)^{T}$ [30]. The terms are transpose of each other. More details in appendix C.

Once the stress fluctuations are calculated, the lattice spin (or lattice rotation rate) at a point \mathbf{x} at time t can be calculated using:

$$\dot{\mathbf{\omega}}^{t}(\mathbf{x}) = \dot{\mathbf{\omega}}^{t(r)} + \delta \dot{\mathbf{\omega}}^{t(\delta\sigma)}(\mathbf{x}) + \delta \dot{\mathbf{\omega}}^{t(\delta\tau)}(\mathbf{x}), \tag{28}$$

where $\dot{\boldsymbol{\omega}}^{t(r)}$ is the mean lattice rotation rate, $\delta \dot{\boldsymbol{\omega}}^{t(\delta\sigma)}(\mathbf{x})$ is the spin fluctuations due to stress fluctuations and $\delta \dot{\boldsymbol{\omega}}^{t(\delta r)}(\mathbf{x})$ is the lattice fluctuations caused by the misorientation fluctuations. The fluctuation terms in Eq. (28) can be rewritten with the first order Taylor expansion approximation as [30]:

$$\dot{\boldsymbol{\omega}}^{t}(\mathbf{x}) = \dot{\boldsymbol{\omega}}^{t(r)} + \frac{\partial \dot{\boldsymbol{\omega}}}{\partial \sigma} \Big|_{\boldsymbol{\sigma}^{(r)}, \overline{\mathbf{g}}^{(r)}}^{t} \delta \boldsymbol{\sigma}^{t}(\mathbf{x}) + \frac{\partial \dot{\boldsymbol{\omega}}}{\partial \delta \mathbf{r}} \Big|_{\boldsymbol{\sigma}^{(r)}, \overline{\mathbf{g}}^{(r)}}^{t} \delta \mathbf{r}^{t}(\mathbf{x}), \tag{29}$$

The second moment of lattice rotation rate is expressed by:

$$\langle \dot{\boldsymbol{\omega}}^{t} \otimes \dot{\boldsymbol{\omega}}^{t} \rangle^{(r)} = \dot{\boldsymbol{\omega}}^{t(r)} \otimes \dot{\boldsymbol{\omega}}^{t(r)} + \langle \delta \dot{\boldsymbol{\omega}}^{t(\delta\sigma)} \otimes \delta \dot{\boldsymbol{\omega}}^{t(\delta\sigma)} \rangle^{(r)} + \langle \delta \dot{\boldsymbol{\omega}}^{t(\deltar)} \otimes \delta \dot{\boldsymbol{\omega}}^{t(\deltar)} \rangle^{(r)} + \\ + \langle \delta \dot{\boldsymbol{\omega}}^{t(\delta\sigma)} \otimes \delta \dot{\boldsymbol{\omega}}^{t(\deltar)} \rangle^{(r)} + \langle \delta \dot{\boldsymbol{\omega}}^{t(\deltar)} \otimes \delta \dot{\boldsymbol{\omega}}^{t(\delta\sigma)} \rangle^{(r)}. \tag{30}$$

The last two terms are transpose relative to each other and represent the cross-covariance of lattice spin fluctuations by stress and lattice spin fluctuations by misorientations. The terms are expressed as:

$$\langle \delta \dot{\boldsymbol{\omega}}^{t(\delta\sigma)} \otimes \delta \dot{\boldsymbol{\omega}}^{t(\delta r)} \rangle^{(r)} = \frac{\partial \dot{\boldsymbol{\omega}}}{\partial \sigma} \Big|_{\boldsymbol{\sigma}^{(r)}, \overline{\boldsymbol{\omega}}^{(r)}}^{t} \langle \delta \boldsymbol{\sigma}^{t} \otimes \delta \mathbf{r}^{t} \rangle^{(r)} \left(\frac{\partial \dot{\boldsymbol{\omega}}}{\partial \delta \mathbf{r}} \Big|_{\boldsymbol{\sigma}^{(r)}, \overline{\boldsymbol{\omega}}^{(r)}}^{t} \right)^{T}, \tag{31}$$

where $\langle \delta \mathbf{\sigma}^t \otimes \delta \mathbf{r}^t \rangle^{(r)}$ is given by:

$$\langle \delta \mathbf{\sigma}^t \otimes \delta \mathbf{r}^t \rangle^{(r)} = \langle \delta \mathbf{\sigma}^{t(\bar{q})} \otimes \delta \mathbf{r}^t \rangle^{(r)} + \frac{\partial \mathbf{\sigma}}{\partial \delta \mathbf{r}} \Big|_{\mathbf{\sigma}^{(r)}, \overline{\mathbf{q}}^{(r)}}^t \langle \delta \mathbf{r}^t \otimes \delta \mathbf{r}^t \rangle^{(r)} . \tag{32}$$

The second and third terms of Eq. (30) are the second moments of lattice rotation rate fluctuations caused by intragranular stress fluctuations and misorientation fluctuations respectively and can be expressed as:

$$\langle \delta \dot{\boldsymbol{\omega}}^{t(\delta\sigma)} \otimes \delta \dot{\boldsymbol{\omega}}^{t(\delta\sigma)} \rangle^{(r)} = \frac{\partial \dot{\boldsymbol{\omega}}}{\partial \sigma} \Big|_{\boldsymbol{\sigma}^{(r)}, \overline{\boldsymbol{q}}^{(r)}}^{t} \langle \delta \boldsymbol{\sigma}^{t(\overline{q})} \otimes \delta \boldsymbol{\sigma}^{t(\overline{q})} \rangle^{(r)} \left(\frac{\partial \dot{\boldsymbol{\omega}}}{\partial \sigma} \Big|_{\boldsymbol{\sigma}^{(r)}, \overline{\boldsymbol{q}}^{(r)}}^{t} \right)^{T}$$
(33)

$$\langle \delta \dot{\boldsymbol{\omega}}^{t(\delta r)} \otimes \delta \dot{\boldsymbol{\omega}}^{t(\delta r)} \rangle^{(r)} = \frac{\partial \dot{\boldsymbol{\omega}}}{\partial \delta r} \Big|_{\boldsymbol{\sigma}^{(r)}, \overline{\mathbf{q}}^{(r)}}^{t} \langle \delta \mathbf{r}^{t} \otimes \delta \mathbf{r}^{t} \rangle^{(r)} \left(\frac{\partial \dot{\boldsymbol{\omega}}}{\partial \delta r} \Big|_{\boldsymbol{\sigma}^{(r)}, \overline{\mathbf{q}}^{(r)}}^{t} \right)^{T}. \tag{34}$$

2.3 Misorientation fluctuations and grain fragmentation

We can use the available information on the second moments of lattice spin to derive expression for integration of lattice rotation rate fluctuations from time t to $t + \Delta t$ within grain r by Taylor expansion approximation [30]. The orientation update from time t to $t + \Delta t$ at point \mathbf{x} is given by:

$$\mathbf{q}^{t+\Delta t}(\mathbf{x}) = \mathbf{q}_{inc}^t(\mathbf{x})\mathbf{q}^t(\mathbf{x}),\tag{35}$$

where $\mathbf{q}^t(\mathbf{x})$ and $\mathbf{q}^{t+\Delta t}(\mathbf{x})$ are the active rotations that rotate sample frame into local crystal frame at time t and $t + \Delta t$ respectively. $\mathbf{q}^t_{inc}(\mathbf{x})$ is the active increment in rotation at time t.

The orientations $\mathbf{q}^t(\mathbf{x})$ and $\mathbf{q}^{t+\Delta t}(\mathbf{x})$ can be expressed as follows:

$$\mathbf{q}^{t}(\mathbf{x}) = \delta \mathbf{q}^{t}(\mathbf{x}) \overline{\mathbf{q}}^{t(r)}, \tag{36A}$$

$$\mathbf{q}^{t+\Delta t}(\mathbf{x}) = \delta \mathbf{q}^{t+\Delta t}(\mathbf{x}) \overline{\mathbf{q}}^{t+\Delta t(r)}, \tag{36B}$$

where the quantities with bar at top are the mean orientations and quantities having δ in front are the misorientations with respect to the mean orientations.

The active increment in rotation term, $\mathbf{q}_{inc}^t(\mathbf{x})$ from Eq. (35) can also be written as the composition of mean rotation increment, $\overline{\mathbf{q}}_{inc}^{t(r)}$ and misorientation increment, $\delta \mathbf{q}_{inc}^t(\mathbf{x})$ with respect to mean rotation increment.

$$\mathbf{q}_{inc}^{t}(\mathbf{x}) = \delta \mathbf{q}_{inc}^{t}(\mathbf{x}) \overline{\mathbf{q}}_{inc}^{t(r)}. \tag{37}$$

Substituting Eq. (37) into Eq. (35) we get the updated orientation at time $t + \Delta t$:

$$\mathbf{q}^{t+\Delta t}(\mathbf{x}) = \delta \mathbf{q}_{inc}^t(\mathbf{x}) \overline{\mathbf{q}}_{inc}^{t(r)} \mathbf{q}^t(\mathbf{x}). \tag{38}$$

After substituting Eq. (36A) in Eq. (38), we get:

$$\mathbf{q}^{t+\Delta t}(\mathbf{x}) = \left(\delta \mathbf{q}_{inc}^{t}(\mathbf{x}) \overline{\mathbf{q}}_{inc}^{t(r)}\right) \left(\delta \mathbf{q}^{t}(\mathbf{x}) \overline{\mathbf{q}}^{t(r)}\right). \tag{39}$$

Equating Eq. (38) and Eq. (36B) we have:

$$\delta \mathbf{q}^{t+\Delta t}(\mathbf{x}) \overline{\mathbf{q}}^{t+\Delta t(r)} = \left(\delta \mathbf{q}_{inc}^{t}(\mathbf{x}) \overline{\mathbf{q}}_{inc}^{t(r)}\right) \left(\delta \mathbf{q}^{t}(\mathbf{x}) \overline{\mathbf{q}}^{t(r)}\right)$$
(40)

Multiplying both sides of Eq. (40) by $\overline{\mathbf{q}}^{t+\Delta t(r)^{-1}}$ and considering $\overline{\mathbf{q}}^{t+\Delta t(r)} = \overline{\mathbf{q}}_{inc}^{t(r)} \overline{\mathbf{q}}^{t(r)}$ we get:

$$\delta \mathbf{q}^{t+\Delta t}(\mathbf{x}) = \delta \mathbf{q}_{inc}^{t}(\mathbf{x}) \overline{\mathbf{q}}_{inc}^{t(r)} \delta \mathbf{q}^{t}(\mathbf{x}) \overline{\mathbf{q}}_{inc}^{t(r)^{-1}} = \delta \mathbf{q}_{inc}^{t}(\mathbf{x}) \delta \mathbf{q}^{t,rot}(\mathbf{x}), \tag{41}$$

where $\delta \mathbf{q}^{t,rot}(\mathbf{x})$ is rotated misorientation at time t given by $\delta \mathbf{q}^{t,rot}(\mathbf{x}) = \overline{\mathbf{q}}_{inc}^{t(r)} \delta \mathbf{q}^{t}(\mathbf{x}) \overline{\mathbf{q}}_{inc}^{t(r)^{-1}}$.

Now, performing a first order Taylor expansion, the misorientation update of Eq.41 can be linearized as [29]:

$$\delta \mathbf{q}^{t+\Delta t}(\mathbf{x}) \approx \delta \mathbf{q}_{inc}^t(\mathbf{x}) + \delta \mathbf{q}^{t,rot}(\mathbf{x}) - \mathbf{I}^q, \tag{42}$$

where I^q is the identity rotation quaternion. Eq. (42) can be expressed by vector parts as:

$$\delta \mathbf{r}^{t+\Delta t}(\mathbf{x}) = \delta \mathbf{r}^{t,rot}(\mathbf{x}) + \delta \mathbf{r}_{inc}^{t}(\mathbf{x}). \tag{43}$$

The second moment of misorientation at time $t + \Delta t$ is given as:

$$\langle \delta \mathbf{r}^{t+\Delta t} \otimes \delta \mathbf{r}^{t+\Delta t} \rangle^{(r)} = \langle \delta \mathbf{r}_{inc}^t \otimes \delta \mathbf{r}_{inc}^t \rangle^{(r)} + \langle \delta \mathbf{r}^{t,rot} \otimes \delta \mathbf{r}_{inc}^t \rangle^{(r)} + \langle \delta \mathbf{r}_{inc}^t \otimes \delta \mathbf{r}^{t,rot} \rangle^{(r)} + \langle \delta \mathbf{r}^{t,rot} \otimes \delta \mathbf{r}^{t,rot} \rangle^{(r)}.$$

$$(44)$$

The terms on the right hand side are given as [30]:

$$\langle \delta \mathbf{r}_{inc}^t \otimes \delta \mathbf{r}_{inc}^t \rangle^{(r)} = \frac{\Delta t^2}{4} \langle \delta \dot{\boldsymbol{\omega}}^{t(\delta\sigma)} \otimes \delta \dot{\boldsymbol{\omega}}^{t(\delta\sigma)} \rangle^{(r)}$$
(45)

$$\langle \delta \mathbf{r}^{t,rot} \otimes \delta \mathbf{r}^{t,rot} \rangle^{(r)} = \overline{\mathbf{R}}_{inc}^{t(r)} \langle \delta \mathbf{r}^{t} \otimes \delta \mathbf{r}^{t} \rangle^{(r)} \overline{\mathbf{R}}_{inc}^{t(r)}$$

$$(46)$$

$$\langle \delta \mathbf{r}^{t,rot} \otimes \delta \mathbf{r}^{t}_{inc} \rangle^{(r)} = \overline{\mathbf{R}}^{t(r)}_{inc} \langle \delta \mathbf{r}^{t} \otimes \delta \boldsymbol{\sigma}^{t} \rangle^{(r)} \left(\frac{\partial \dot{\boldsymbol{\omega}}}{\partial \boldsymbol{\sigma}} \Big|_{\boldsymbol{\sigma}^{(r)}, \overline{\boldsymbol{\omega}}^{(r)}}^{t} \right)^{T} \frac{\Delta t}{2} +$$

$$\overline{\mathbf{R}}_{inc}^{t,(r)} \langle \delta \mathbf{r}^t \otimes \delta \mathbf{r}^t \rangle^{(r)} \left(\frac{\partial \dot{\boldsymbol{\omega}}}{\partial \delta \mathbf{r}} \Big|_{\boldsymbol{\sigma}^{(r)} \, \overline{\boldsymbol{\sigma}}^{(r)}}^t \right)^T \frac{\Delta t}{2}, \tag{47}$$

where $\overline{\mathbf{R}}_{inc}^{t(r)}$ is the rotation matrix representation of mean increment in rotation, $\overline{\mathbf{q}}_{inc}^{t(r)}$.

The misorientation spreads, Eq. (44) may become large with plastic strains so that it is not possible to represent the misorientation with just one mean value along with one second moment. Therefore, a grain fragmentation model becomes necessary. In our formulation a parent grain is subdivided into two child grains once the intragranular misorientation spread per grain reaches a critical value [30]. The fragmented child grains initialized with parent state variables evolve separately in the next deformation steps. We chose to quantify the magnitude of intragranular

orientation spreads using an equivalent isotropic spread, which is a scalar parameter defined as: $SD = \sqrt[3]{SD_1 \times SD_2 \times SD_3}$ [81] with $SD_i = \sqrt{\lambda^i}$, where λ^i are the principal values with directions, \mathbf{v}^i of the misorientation distribution, $\langle \delta \mathbf{r} \otimes \delta \mathbf{r} \rangle^{(r)}$, Eq. (44).

Misorientation distribution of a parent grain described by its mean value, $\langle \delta \mathbf{r} \rangle^{(r)} = 0$ and its second moment, $(\delta \mathbf{r} \otimes \delta \mathbf{r})^{(r)}$, needs to be divided into two distributions for two equally weighted child grains. Each needs to have a mean value, $\langle \delta \mathbf{r} \rangle_{f_i}^{(r)}$, and a second moment, $\langle \delta \mathbf{r} \otimes \delta \mathbf{r} \rangle_{f_i}^{(r)}$. At first, the eigenvalues and eigenvectors of the parent's misorientation distribution, $\langle \delta \mathbf{r} \otimes \delta \mathbf{r} \rangle^{(r)}$ are calculated and arranged in descending order as: $\mathbf{E} = [\lambda^1, \lambda^2, \lambda^3]$ and $\mathbf{V} = [\mathbf{v}^1, \mathbf{v}^2, \mathbf{v}^3]$. The distribution along the direction of largest variation, \mathbf{v}^1 , can be divided separately from the other two principal distributions. The misorientation between two orientations along largest principal direction, \mathbf{v}^1 is calculated using $\alpha = 4\sin^{-1}\left(2\sqrt{\frac{\lambda^1}{2\pi}}\right)$. When α becomes greater than a selected

critical fragmentation angle (set as 15° for all simulation in the present work or equivalently $SD_1 =$ 0.082), the parent grain is divided into two child grains or fragments. The mean misorientations of the fragments relative to the mean orientation of the parent are [82, 83]:

$$\langle \delta \mathbf{r} \rangle_{f_1}^{(r)} = -2 \sqrt{\frac{\lambda^1}{2\pi}} \mathbf{v}^1; \quad \langle \delta \mathbf{r} \rangle_2^{(r)} = 2 \sqrt{\frac{\lambda^1}{2\pi}} \mathbf{v}^1. \tag{48}$$

The misorientations are also:

$$\langle \delta \mathbf{q} \rangle_{f_1}^{(r)} = \begin{cases} \sqrt{\frac{1 - \langle \delta \mathbf{r} \rangle_{f_1}^{(r)} \cdot \langle \delta \mathbf{r} \rangle_{f_1}^{(r)}}{\langle \delta \mathbf{r} \rangle_{f_1}^{(r)}}} ; \ \langle \delta \mathbf{q} \rangle_{f_2}^{(r)} = \begin{cases} \sqrt{\frac{1 - \langle \delta \mathbf{r} \rangle_{f_2}^{(r)} \cdot \langle \delta \mathbf{r} \rangle_{f_2}^{(r)}}{\langle \delta \mathbf{r} \rangle_{f_2}^{(r)}}} \end{cases} . \tag{49}$$

The mean orientations of fragments are then given by:

$$\overline{\mathbf{q}}_{f_1}^{(r)} = \langle \delta \mathbf{q} \rangle_{f_1}^{(r)} \overline{\mathbf{q}}^{(r)}; \overline{\mathbf{q}}_{f_2}^{(r)} = \langle \delta \mathbf{q} \rangle_{f_2}^{(r)} \overline{\mathbf{q}}^{(r)}. \tag{50}$$

The second moments of fragments in the principal frame of parent's distribution are given as:

The second moments of fragments in the principal frame of parent's distribution are given as:
$$\langle \delta \mathbf{r} \otimes \delta \mathbf{r} \rangle_{f_1}^{(r),p} = \langle \delta \mathbf{r} \otimes \delta \mathbf{r} \rangle_{f_2}^{(r),p} = \begin{bmatrix} \lambda^1 \left(1 - \frac{2}{\pi} \right) & 0 & 0 \\ 0 & \lambda^2 & 0 \\ 0 & 0 & \lambda^3 \end{bmatrix}.$$
(51)

The second moments of the fragments in sample frame are obtained by the simple coordinate transformation as:

$$\langle \delta \mathbf{r} \otimes \delta \mathbf{r} \rangle_{f_1}^{(r)} = \langle \delta \mathbf{r} \otimes \delta \mathbf{r} \rangle_{f_2}^{(r)} = \mathbf{V} \langle \delta \mathbf{r} \otimes \delta \mathbf{r} \rangle_{f_1}^{(r),p} \mathbf{V}^T.$$
 (52)

The grain fragmentations are considered in the physical space and not only in the orientation space by division of intragranular orientation space as in our earlier work [30]. To this end, grain size (diameter) of the fragmented grains is calculated. The total volume of the initial material, V_{tot} , is calculated assuming that each grain has spherical shape and same grain diameter as:

$$V_{tot} = n_{gr} \frac{1}{6} \pi D_i^3, \tag{53}$$

where n_{gr} is the total number of initial equally weighted grains at the start of the simulation and D_i is the initial diameter of grains. At any strain increment, the diameter of any grain, $D_g^{(r)}$ can be calculated from its weight, $w^{(r)}$ using:

$$D_g^{(r)} = 2\left(w^{(r)}\frac{3V_{tot}}{4\pi}\right)^{1/3}. (54)$$

During plastic deformation, a fraction of grains develops divergent regions relative to the parent orientation. Such orientation subdivision causes deformation bands. Thin regions between the deformation bands are called transition bands. The orientation spreads of such bands are typically bi-modal meaning that the orientations are clustered around two distinct stable regions, which also have some misorientation spreads. In the FF-VPSC model, a grain is bi-modal if it forms a transition band. Next, the criteria for a transition band formation i.e. a grain to be called bi-modal is described.

In the FF-VPSC model, at any strain increment, a parent grain can be fragmented into two child grains each having half of the weight of its parent, as described earlier. In the next step, each of these two children will act as independent grain (parent grain) which may further be fragmented if the fragmentation criteria are fulfilled. As a result, an initial parent grain can be subdivided into large numbers of child grains at a large deformation level. It is to be noted that, in our model, we determine if a grain is bi-modal or form a transition band for initial parent grain only and not for any child grains. In other words, we identify the bimodality for initial grains only. The reason is our recrystallization model, which will be described shortly In order to determine a transition band formation i.e. whether the grain is bimodal, all sub grains of a parent grain are stacked/merged together and mean orientation of parent grain, $\overline{\mathbf{q}}^{(r),tot}$ is calculated, the value of which depends on all orientation of subdivided grains. Then mean second moment of misorientation of the grain $\langle \delta \mathbf{r} \otimes \delta \mathbf{r} \rangle^{(r),tot}$ is calculated taking the vector part of $\overline{\mathbf{q}}^{(r),tot}$. Next, eigen values λ^1 , λ^2 , λ^3 and eigen vectors \mathbf{v}^1 , \mathbf{v}^2 , \mathbf{v}^3 of $\langle \delta \mathbf{r} \otimes \delta \mathbf{r} \rangle^{(r),tot}$ are calculated and arranged in the descending order. Now, a set of discrete intervals are sampled along the dominant rotation axis \mathbf{v}^1 of the initial parent grain. Probability density functions of SD_1 along the dominant rotation axis are calculated over the discrete intervals. Next, the shape of the distribution is assessed. If there are two larger peaks of the distribution separated by a smaller peak in between, the parent grain is tagged as a bi-modal grain forming a transition band. This parent grain forming a transition band serves as suitable spot for transition band nucleation and orientation of the nucleus is taken from the transition band region in the recrystallization model. In contrast, if misorientation spreads are more uniform in every direction such that there is no bi-modal separation in the misorientation distribution but only unimodal, these grains will influence the grain boundary nucleation kinetics in the recrystallization model.

2.4 Recrystallization model

The process of recrystallization involves nucleation of new grains in deformed microstructures and their growth, which happens during annealing at a given temperature for a given time [40, 84]. Intragranular orientation gradients and strain energy of the microstructure drive the nucleation of new grains during recrystallization [40, 85]. The growth of the nucleus takes place by migration of high-angle grain boundaries influenced by the difference of strain energies of two sides of the boundary. Therefore, modeling of recrystallization is only possible after accurate modeling of plastic deformation. The nucleation and growth kinetics sub-models are developed based on the quantities calculated using FF-VPSC. The formulation of intragranular orientation gradients and strain energy are briefly summarized according to [31]. Two nucleation processes of grain boundary nucleation and transition band nucleation are also presented.

2.4.1 Intragranular orientation gradients and strain energy

An expression for calculating the intragranular orientation gradients based on a known quantity, the second moment of misorientation vectors, $\langle \delta \mathbf{r} \otimes \delta \mathbf{r} \rangle^{(r)}$ was developed in [31].

Let us consider a reference misorientation vector, $\delta \mathbf{r}^{ref}$ and a misorientation vector, $\delta \mathbf{r}$ which is a spatially neighboring point with respect to the reference point within a grain. The misorientation between these two points is: $\delta \mathbf{r}^{loc} \approx \delta \mathbf{r} - \delta \mathbf{r}^{ref}$. An expression for the first and second moment of $\delta \mathbf{r}^{loc}$ can be formulated as [31]:

$$\langle \delta \mathbf{r}^{loc} \rangle^{(r)} = \mathbf{0},\tag{55}$$

$$\langle \delta \mathbf{r}^{loc} \otimes \delta \mathbf{r}^{loc} \rangle^{(r)} = \left(\langle \delta \mathbf{r} \otimes \delta \mathbf{r} \rangle^{(r)^{-1}} + \frac{1}{\alpha} \mathbf{I} \right)^{-1} \langle \delta \mathbf{r} \otimes \delta \mathbf{r} \rangle^{(r)^{-T}} \left(\langle \delta \mathbf{r} \otimes \delta \mathbf{r} \rangle^{(r)^{-1}} + \frac{1}{\alpha} \mathbf{I} \right)^{-T} + \left(\langle \delta \mathbf{r} \otimes \delta \mathbf{r} \rangle^{(r)^{-1}} + \frac{1}{\alpha} \mathbf{I} \right)^{-1}, \tag{56}$$

where **I** is the identity matrix, α is the variance which controls the magnitude of misorientation angle of the local neighbor. When $\alpha \to 0$, the second moment $\langle \delta \mathbf{r}^{loc} \otimes \delta \mathbf{r}^{loc} \rangle^{(r)} \to 0$, while when $\alpha \to \infty$, $\langle \delta \mathbf{r}^{loc} \otimes \delta \mathbf{r}^{loc} \rangle^{(r)} \to 2 \langle \delta \mathbf{r} \otimes \delta \mathbf{r} \rangle^{(r)}$ all possible local neighbor misorientation distributions are included. In this study, we assume $\alpha \to \infty$ resulting in $\langle \delta \mathbf{r}^{loc} \otimes \delta \mathbf{r}^{loc} \rangle^{(r)} = 2 \langle \delta \mathbf{r} \otimes \delta \mathbf{r} \rangle^{(r)}$. Then, the local neighbor misorientations distribution can be defined by $\langle \delta \mathbf{r}^{loc} \rangle^{(r)}$.

The misorientation angle between two neighboring material points, $\delta\theta$ can be defined (using small angle approximation) as:

$$\delta\theta \approx 2|\delta \mathbf{r}^{loc}|,$$
 (57)

where | | defines the length of the misorientation vector. The average misorientation angle of the local neighbors is given by:

$$\langle \delta \theta \rangle^{(r)} \approx 2 \langle |\delta \mathbf{r}^{loc}| \rangle^{(r)} = 2 \langle \sqrt{\delta \mathbf{r}^{loc} \cdot \delta \mathbf{r}^{loc}} \rangle^{(r)} \approx 2 \sqrt{2\mathbf{I} \cdot \langle \delta \mathbf{r} \otimes \delta \mathbf{r} \rangle^{(r)}}.$$
 (58)

The strain energy in a grain is given by [35, 86, 87]:

$$E^{(r)} = \rho^{(r)} \mu b^2 / 2,\tag{59}$$

where b is the Burgers vector, μ is the shear modulus, $\rho^{(r)}$ is the dislocation density in the grain r. The increase of slip resistance due to hardening is proportional to the square root of the accumulated dislocation density, $\sum_{s} \left(\tau_{c}^{s,(r)} - \tau_{c,0}^{s,(r)}\right) \sim \sqrt{\rho^{(r)}}$. Then, the strain energy can be written as [35]:

$$E^{(r)} \sim \sum_{s} \left(\tau_c^{s,(r)} - \tau_{c,0}^{s,(r)} \right)^2. \tag{60}$$

The calculated dislocation density which is the sum of statistically stored dislocation (SSD) and geometrically necessary dislocation (GND), is related only to the accumulated shear strain on slip systems in the grain. In this study, we make no distinction between SSD and GND densities, although more accurate approach would be calculating GNDs from intragranular orientation spread or strain-field distributions, while SSDs would evolve separately. This separate treatment of GND densities will be the subject of future works, which in turn will affect the recrystallization through work hardening and stored strain energy.

We adopt a Voce-type hardening law and make it simply linear for all simulation cases presented in the paper based on: $\tau_0^s = 1$ MPa, $\tau_1^s = 0$ MPa, $\theta_0^s = 1$ MPa, $\theta_1^s = 1$ MPa.

$$\tau_c^{s,(r)} = \tau_0^s + \left(\tau_1^s + \theta_1^s \sum_{s'} \gamma^{s',(r)}\right) \left(1 - exp\left(-\sum_{s'} \gamma^{s',(r)} \left| \frac{\theta_0^s}{\tau_1^s} \right| \right)\right)$$

$$\tag{61}$$

2.4.2 Grain boundary and transition band nucleation mechanisms

Experimental observations are that nucleation usually occurs at grain boundaries and transition bands in deformed structures, while grain grown is driven by the difference in stored energy [40, 85]. For grain boundary nucleation, the local neighbor misorientation angle and strain energy per grain are assumed to be proportional to the mean neighbor misorientation angle, $\langle \delta \theta \rangle^{(r)}$ and mean strain energy, $E^{(r)}$ of the grain. To nucleate a new grain, the given grain must have a critical local neighbor misorientation angle, $\delta \theta_{th}^{gb}$, and a critical strain energy, E_{th}^{gb} . In our simulations, we set $E_{th}^{gb} = 0$ meaning that even very minimal strain energy is sufficient for nucleation.

Let us consider the probability of grain boundary nucleation for a grain of weight $w^{(r)}$ in time Δt . The grain with an area, A is subdivided into large number of small areas dA having weight dw. The probability of forming a grain boundary nucleus of the area dA is [31, 35, 88]:

$$P_{gb}^{(r)}(\Delta t, w^{(r)}, E^{(r)}) = 1 - \left(1 - B_{gb} \exp\left(-\frac{A_{gb}}{E^{(r)^2}}\right)\right)^{\Delta t \left(\frac{w^{(r)}}{dw}\right)^{2/3}},\tag{62}$$

where B_{gb} is a pre-exponential factor scaling the probability ($B_{gb} \le 1$), A_{gb} is a fitting parameter that determines likelihood of grain boundary nucleation in terms of strain energy. In our simulations, $dw = 10^{-6}$.

After calculating the nucleation probability, it is compared to a random number between 0 and 1. If the probability is greater than the random number, a new grain nucleates having a weight of $w_{nuc} = 0.0001$. The newly nucleated grain has zero strain energy and an initial value of slip resistance taken from the deformation model.

The grain boundary nucleation takes place by a grain boundary sub-grain formation, which bulges out into the neighboring grain. Crystal orientation of the nucleated grain is randomly sampled from the misorientation distribution extremes. The condition for the grain boundary misorientation is [31]: $|\delta \mathbf{r}^{gb}| > c \times SD\left(\frac{\delta \mathbf{r}^{gb}}{|\delta \mathbf{r}^{gb}|}\right)$, where $SD\left(\frac{\delta \mathbf{r}^{gb}}{|\delta \mathbf{r}^{gb}|}\right)$ is the standard deviation in the misorientation direction $\frac{\delta \mathbf{r}^{gb}}{|\delta \mathbf{r}^{gb}|}$, and c is a constant that determines the minimum misorientation angle in degrees between the mean grain orientation and grain boundary orientation.

The nucleation is also observed in the transition bands [43, 89]. Grains often form regions of deformation bands which has large orientation gradients [90]. Transition bands are situated between deformation bands having narrow regions with high orientation gradients making it suitable place for grain nucleation. In this model, the transition bands are identified from misorientation distributions which forms multi-modal orientation distributions [30].

The transition band nucleation happens in grains that form bi-modal misorientation distributions. The local neighbor misorientation angle and strain energy are also considered as proportional to the mean neighbor misorientation angle $\langle \delta \theta \rangle^{(r)}$ and strain energy, $E^{(r)}$ of the given grain. We emphasize that only those grains that have bi-modal misorientation distributions and have sufficient strain energy and local misorientation angle greater than the threshold values: E_{th}^{tb} and $\delta \theta_{th}^{tb}$ can nucleate a new grain. The probability for the transition band nucleation is [31, 35]:

$$P_{tb}^{(r)}(\Delta t, w^{(r)}, E^{(r)}) = 1 - \left(1 - B_{tb} \exp\left(-\frac{A_{tb}}{E^{(r)^2}}\right)\right)^{\frac{\Delta t}{dt}\left(\frac{w^{(r)}}{dw}\right)^{2/3}},\tag{63}$$

where B_{tb} is a pre-exponential factor scaling the probability ($B_{tb} \leq 1$), while A_{tb} is a fitting parameter that determines likelihood of grain boundary nucleation. For each grain having a bimodal distribution, the probability of nucleation at transition band is calculated and then compared to a random number between 0 and 1. If the probability is greater than the random number, a new grain is nucleated. The defect-free grain growth into plastically deformed microstructure.

Grain growth happens by the mobility of a grain boundary when there is difference of stored energy between the two sides of boundary. The boundary should be a high angle grain boundary. Since our mode is mean-field we assume every grain boundary is a high angle boundary. Grains with a

higher strain energy shrink, while grains with lower strain energy grow. The velocity of the grain boundary when it becomes mobile is given by:

$$v = MP, (64)$$

where P is the pressure on the boundary and M is the mobility of the boundary [91]. In FF-VPSC, the boundary velocity of each grain, $v^{(r)}$ is considered proportional to the difference of stored energy of a given grain $E^{(r)}$ and stored energy of the effective medium E^{avg} :

$$v^{(r)} = M\left(E^{avg} - E^{(r)}\right),\tag{65}$$

where $E^{avg} = \sum_r w^{(r)} E^{(r)}$. The change of weight of the grain due to its boundary migration with velocity $v^{(r)}$ from time t to $t + \Delta t$ is given by [35]:

$$w^{(r),t+\Delta t} = w^{(r),t} + 3M \left(\frac{4\pi}{3}\right)^{\frac{1}{3}} \left(w^{(r),t}\right)^{\frac{2}{3}} \left(E^{avg} - E^{(r)}\right) \Delta t. \tag{66}$$

3. Results and discussion

The FF-VPSC with its deformation and recrystallization sub-models is used for the prediction of deformation and recrystallization textures of cubic metals. First, the model is used to simulate formation of Cu-type and brass-type rolling textures to 95% rolling reduction and formation of static recrystallized textures. These predicted textures are compared to those predicted by the full-field viscoplatic fast Fourier transform (VPFFT) [92-96] and standard VPSC models. Next, the deformed and recrystallized textures of Al-5182-O are predicted and compared to experimental results. The recrystallized textures of an AM cobalt-based alloy, MarM-509, are predicted and compared to experimental data. Finally, the deformation after rolling to 85% reduction and recrystallization textures of IF-steel are predicted and verified experimentally.

3.1 Cu-type and brass-type rolling and recrystallization textures of FCC metals

The Cu-type texture features orientation around the ideal $\{211\}\langle \bar{1}11\rangle$ orientation, which is termed as the copper component (Cu) and some orientations around $\{153\}\langle 11\bar{2}\rangle$ [49, 97, 98]. The development of such texture is favored in high SFE metals [99]. On the other hand, the brass-type texture is described mainly by the ideal orientations of $\{110\}\langle \bar{1}12\rangle$, which is termed as the brass components (B) and some intermediate orientations around $\{110\}\langle 1\bar{1}0\rangle$ [49, 97, 100, 101]. The development of such texture is favored in low SFE metals [49, 99]. Appendix A presents locations of these ideal rolling texture components in pole figures.

3.1.1 Cu-type rolling texture and its recrystallization

Rolling of high SFE metal, copper, to 95% reduction and subsequent annealing [97, 102, 103] are simulated using FF-VPSC. A velocity gradient, **L**, to impose the rolling in the model is

$$\mathbf{L} = \begin{bmatrix} 1 & 0 & 0 \\ 0 & 0 & 0 \\ 0 & 0 & -1 \end{bmatrix}. \tag{67}$$

A time increment is selected to provide a strain increment, $\Delta \varepsilon$, of 0.01. For the initial texture to initialize the simulation, we selected 400 randomly orientated equally weighted grains. The grains deform by $\{111\}\langle 1\overline{1}0\rangle$ slip family. Linear hardening of the slip systems is considered, as described earlier. The rolling process is simulated using the plane strain compression (PSC) boundary conditions, Eq. (67). $\{111\}$ and $\{100\}$ poles are presented to visualize texture evolution.

Comparisons of textures simulated by standard VPSC and FF-VPSC are presented in Fig. 1 for the Cu-type texture evolution at different strain levels. The standard VPSC and FF-VPSC models were initialized with the same initial texture and slip systems as well as the same hardening and boundary conditions. The models are different because the FF-VPSC model considers the second moments of micromechanical fields and misorientations spreads causing grain fragmentations, while the standard VPSC model relies on the first moments of micromechanical fields with no intragranular misorientation spreads developing and thus, no grain fragmentation. Starting with 400 initial grains, the FF-VPSC model predicts the total number of grains after fragmentation with equivalent plastic strain to be: 435 ($\varepsilon_{eq} = 0.22$), 647 ($\varepsilon_{eq} = 0.51$), 1091 ($\varepsilon_{eq} = 0.92$), 2001 ($\varepsilon_{eq} = 1.61$), and 3091 ($\varepsilon_{eq} = 3.0$). Future works will attempt to predict the evolution of grain size.

Looking at Fig. 1, both FF-VPSC and standard VPSC simulate the Cu component with no significant differences in intensities up to 80% reduction. At 95% reduction, we observe that the rate of texture evolution is slower using FF-VPSC than standard VPSC. Moreover, comparing $\{111\}$ poles, we observe that the standard VPSC begins to lack of intensities at $(112)[11\bar{1}]$ [97] orientation compared to FF-VPSC.

Fig. 2 compares measured and simulated textures using standard VPSC, FF-VPSC and VPFFT. The initial microstructural cell for the simulation using VPFFT was a periodic Voronoi unit cell shown in the appendix. The same 400 random grain orientations used in the VPSC simulations were assigned to approximately equiaxed grains in the 400 grains Voronoi unit cell. PSC boundary conditions, slip systems, and hardening as in the VPSC simulations were used for the VPFFT simulations. Comparison of the pole figures shows that the FF-VPSC and VPFFT models predict similar texture evolution to very large strains. It is grateful to achieve such predictions using FF-VPSC, which is a much faster code since mean-field than VPFFT. The simulation using VPFFT took 26100 seconds, while that using FF-VPSC took 2528 seconds on a regular desktop computer.

Fig. 3 shows measured [103] and predicted fully recrystallized textures. The predictions are shown based solely on transition band nucleation and based on solely grain boundary nucleation. Evidently, the predicted recrystallized texture based on the nucleation at transition bands captures

the cube component (C) very well consistent with the measured texture. The formation of the cube texture is well known in the literatus [33, 44]. The C component is also depicted in appendix A. The parameters used in the recrystallization model are given in Table 1.

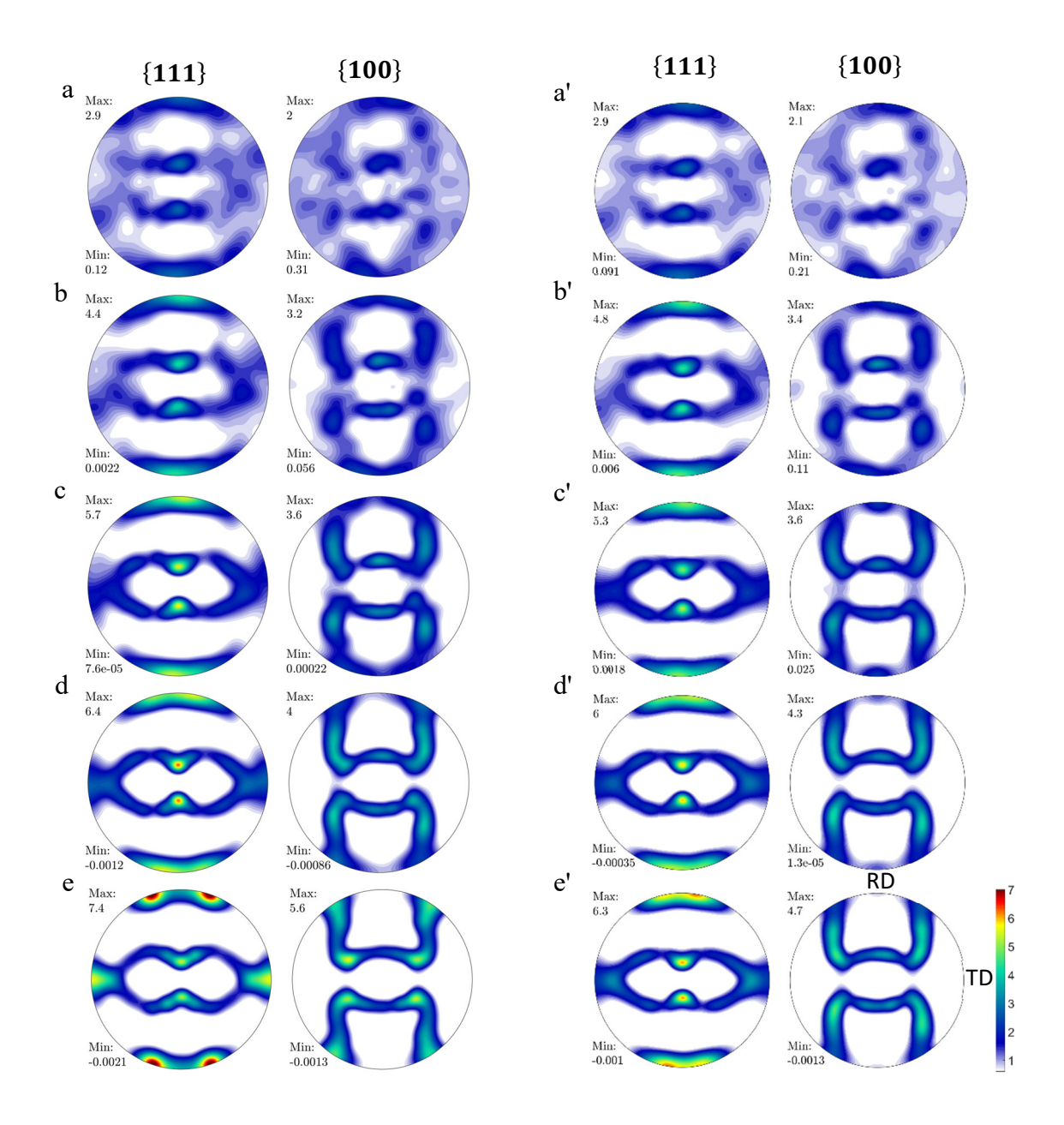


Figure 1. Pole figures showing the evolution of Cu-type texture as predicted using the standard VPSC model during rolling to: (a) 20% (-0.22), (b) 40% (-0.51), (c) 60% (-0.92), (d) 80% (-1.61) and (e) 95% (-3.0) reduction (true strain), respectively. The corresponding results obtained using the FF-VPSC model are shown in a', b', c', d', and e'.

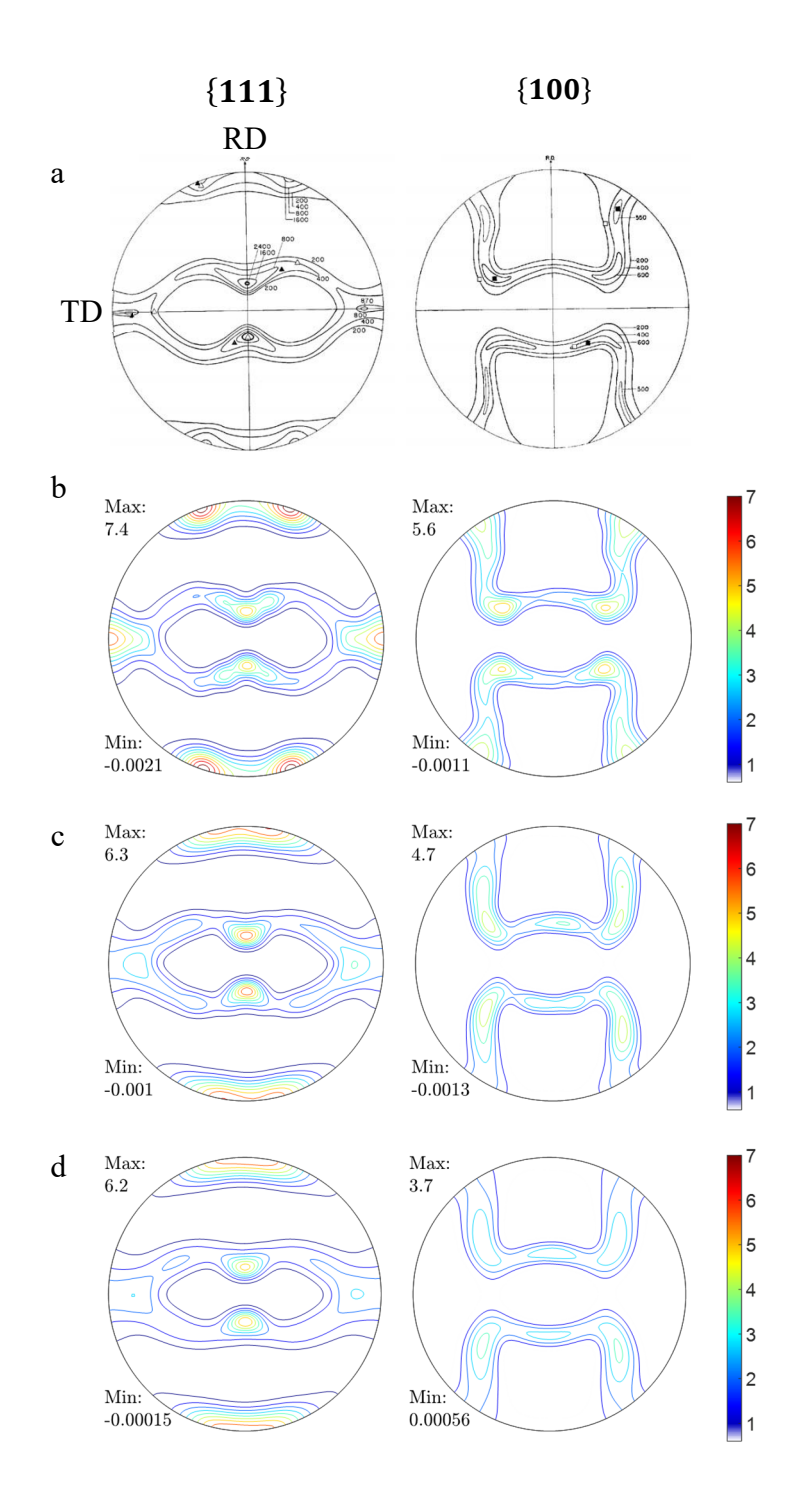


Figure 2. Pole figures comparing the Cu-type texture after rolling to 95% reduction (a) measured deformation texture of 99.99% Cu taken from [49] and predicted deformation texture using (b) standard VPSC, (c) FF-VPSC, and (d) VPFFT.

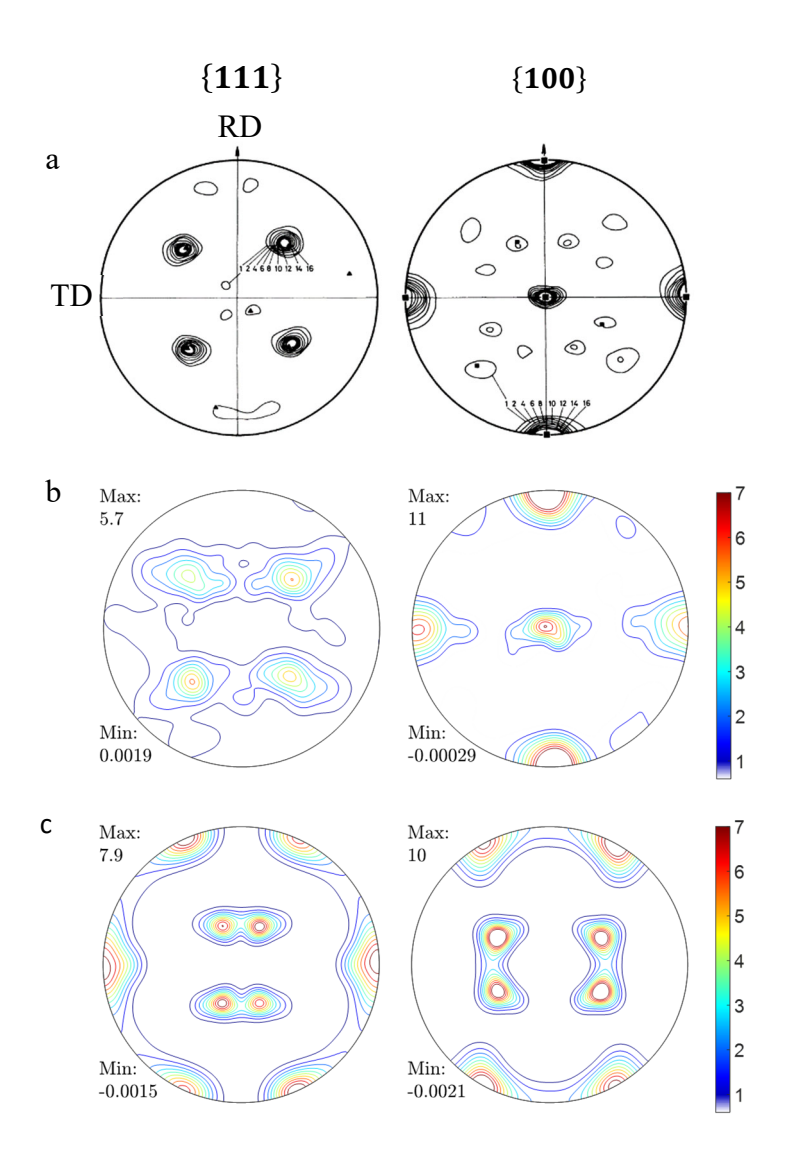


Figure 3. Pole figures showing Cu-type textures after rolling to 95% reduction (Figs. 2a and c) and subsequent recrystallization: (a) measured fully recrystallized texture of 99.99% Cu taken from [103] and predicted fully recrystallized texture based on (b) 100% transition band nucleation and (c) 100% grain boundary nucleation.

3.1.2 Brass-type rolling texture and its recrystallization

For predicting brass-type texture evolution during rolling to 95% reduction and subsequent recrystallization, we use the same initial texture consisting of 400 random orientations as for simulating Cu-type texture evolution and subject it to the same boundary conditions (i.e. Eq. (67). The deformation is carried out using $\{111\}\langle 1\bar{1}0\rangle$ slip and $\{111\}\langle 11\bar{2}\rangle$ twin systems. The twin systems accommodate strain through the pseudo slip and no crystal reorientation is performed for the twinned domains. These simplifications have no appreciable influence on texture evolution considering morphology of twins in the FCC metals [104]. However, accurate modeling of twin

lamellae is important for predicting hardening since twins cause pronounced barrier-type hardening [105]. In our work, the ratio of initial twin (pseudo slip) resistance and initial slip system resistance is set to be 0.8, as in earlier works [58, 63]. The brass-type rolling simulations were performed with the same rolling boundary condition as the Cu-type rolling simulations with linear hardening. {111} and {100} poles are presented next to visualize predicted texture evolution during deformation and recrystallization.

The comparisons of texture evolution for the brass-type texture simulated by standard VPSC and FF-VPSC during rolling to very large strains are presented in Fig. 4. The simulations using FF-VPSC begins with 400 grains but due to modeling of grain fragmentation, the number of grains evolved with equivalent plastic strain as: 412 ($\varepsilon_{eq} = 0.22$), 562 ($\varepsilon_{eq} = 0.51$), 872 ($\varepsilon_{eq} = 0.92$), 1075 ($\varepsilon_{eq} = 1.61$), and 3392 ($\varepsilon_{eq} = 3.0$). Comparing the model performances, we observe that there is no large differences in the predicted texture evolution up to 60% reduction, except that the standard VPSC predicts slightly sharper texture. However, the standard VPSC begins to deviate from the ideal brass-type texture at 80% reduction, which becomes even more prominent at 95% reduction. In contrast, the FF-VPSC continue to predict texture evolution around the ideal B orientations even at very high strain levels. Fig. 5 shows the comparison between standard VPSC, FF-VPSC and VPFFT predictions and experiments. Evidently, the FF-VPSC and VPFFT predictions resemble experiments much better than the standard VPSC model. The consideration of grain fragmentation enables such good predictions of FF-VPSC in a computationally efficient manner.

Fig. 6 shows a measured brass-type texture after 95% rolling reduction followed by subsequent recrystallization. The measured brass-type texture is for a low SFE Ag from [103]. The corresponding pole figures showing the simulated rolled and recrystallized textures using the FF-VPSC model based on the transition band nucleation and grain boundary nucleation mechanisms are also given in the figure. The former shows much better agreement because the transition band nucleation is a predominant nucleation mechanism in the material undergoing recrystallization. It should be noted that even better predictions can be achieved by allowing a few percentages of the grain boundary nucleation. The parameters for the recrystallization model are provided in Table 1.

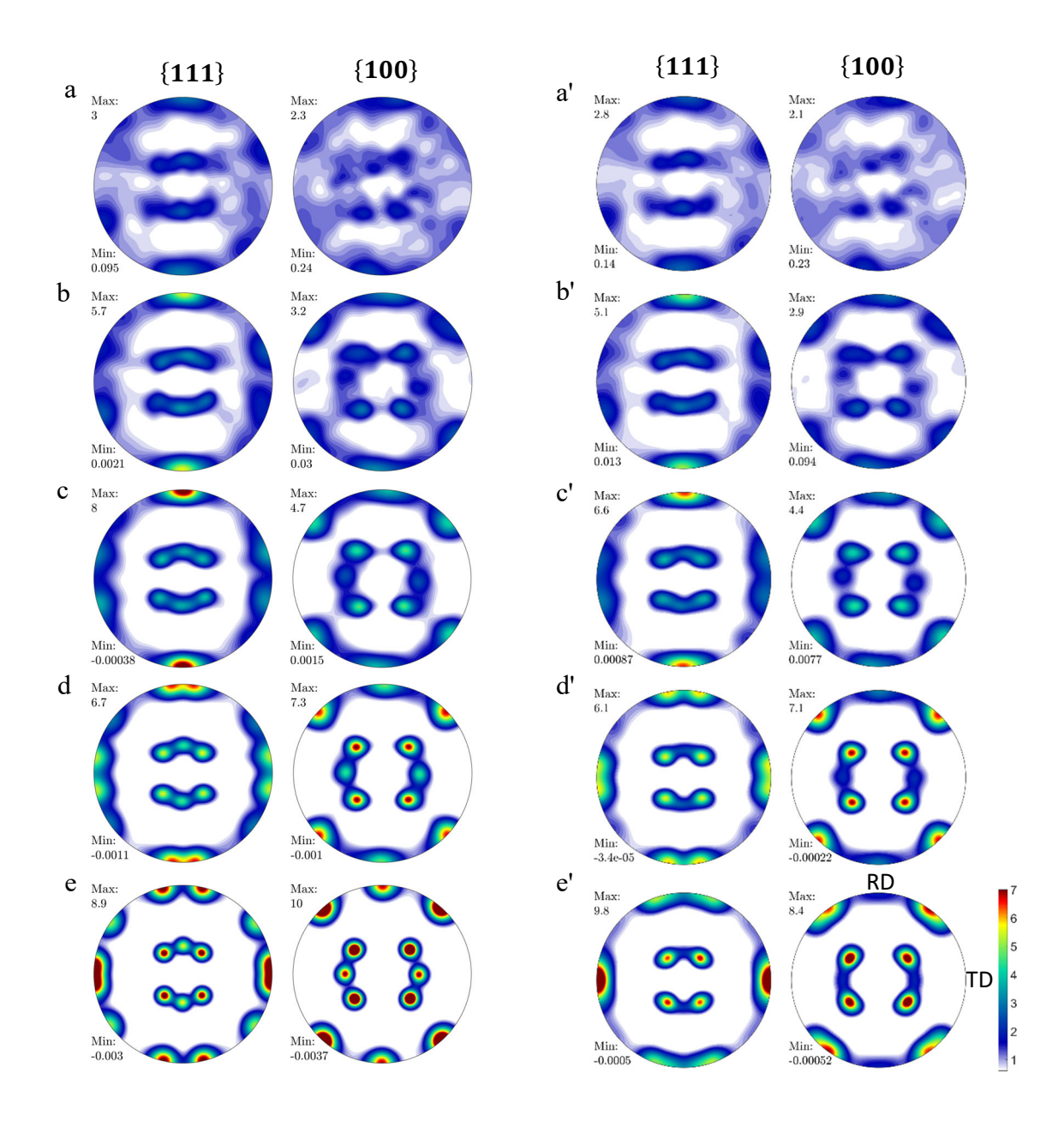


Figure 4. Pole figures showing the evolution of brass-type texture as predicted using the standard VPSC model during rolling to: (a) 20% (-0.22), (b) 40% (-0.51), (c) 60% (-0.92), (d) 80% (-1.61) and (e) 95% (-3.0) reduction (true strain), respectively. The corresponding results obtained using the FF-VPSC model are shown in a', b', c', d', and e'.

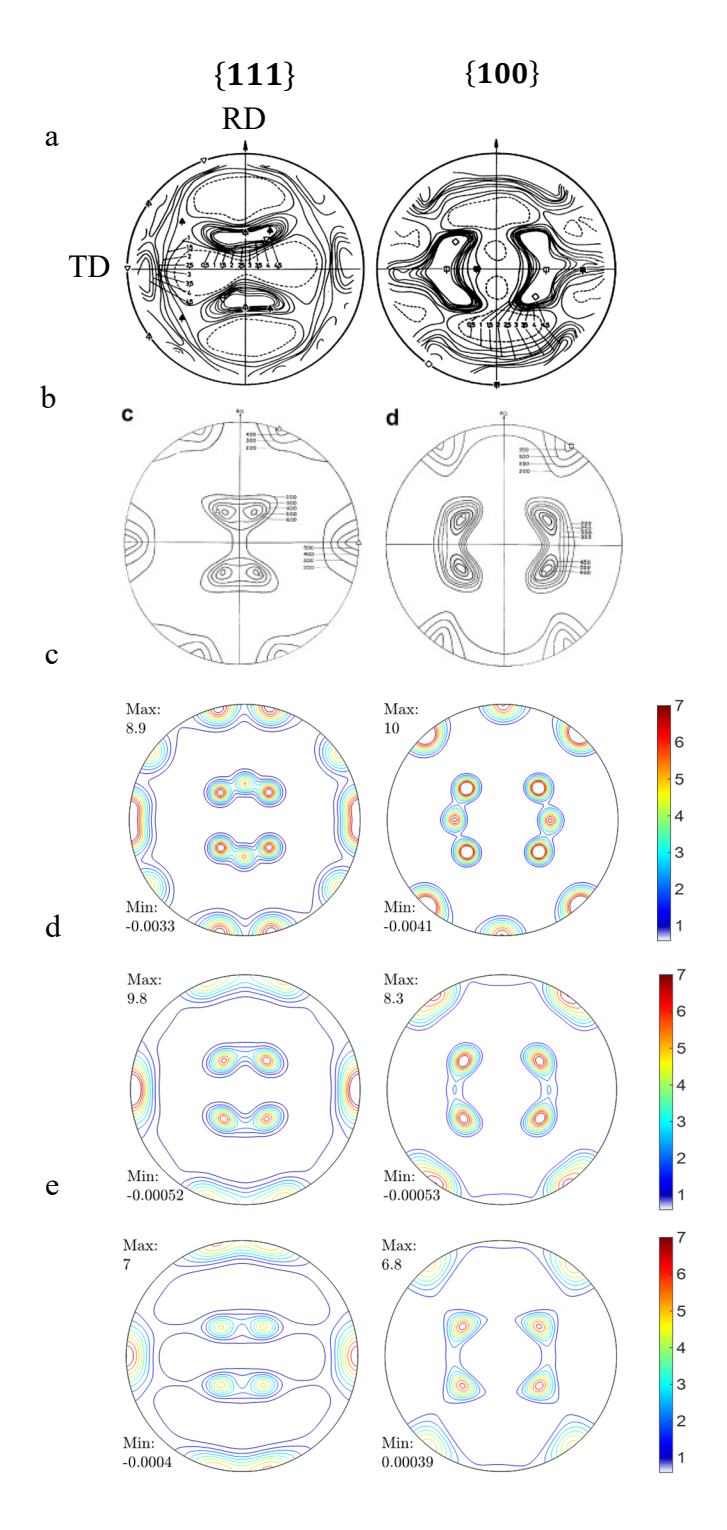


Figure 5. Pole figures comparing the brass-type texture after rolling to 95% reduction (a) measured deformation texture of 99.999% Ag taken from [103], (b) measured deformation texture of brass (with 30% zinc) taken from [49] and predicted deformation texture using (c) standard VPSC, (d) FF-VPSC, and (e) VPFFT.

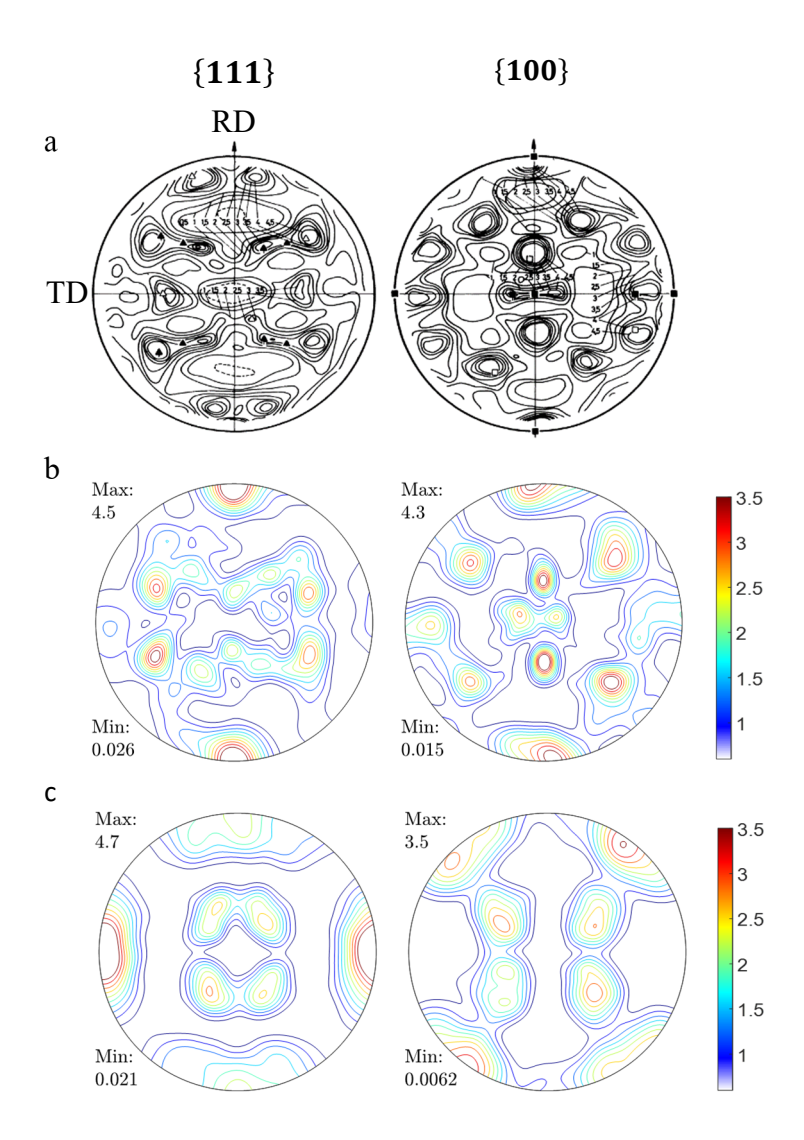


Figure 6. Pole figures showing brass-type textures after rolling to 95% reduction (Figs. 5a and d) and subsequent recrystallization: (b) measured fully recrystallized texture of 99.999% Ag taken from [103] and corresponding predicted fully recrystallized texture based on (b) 100% transition band nucleation, (c) 100% grain boundary nucleation.

Fig. 7 compares the probability density functions (pdfs) of equivalent isotropic spreads (SD) developing for the Cu-type and brass-type textures during rolling at several strain levels. The magnitude of isotropic spreads increases with increase in the strain levels. Initially, the spreads are slightly larger for the Cu-type texture but later become similar. The spreads saturate at large strains. Note the presented spreads include both unimodal and bi-modal misorientation distributions of the 400 weighted parent grains and their fragments.

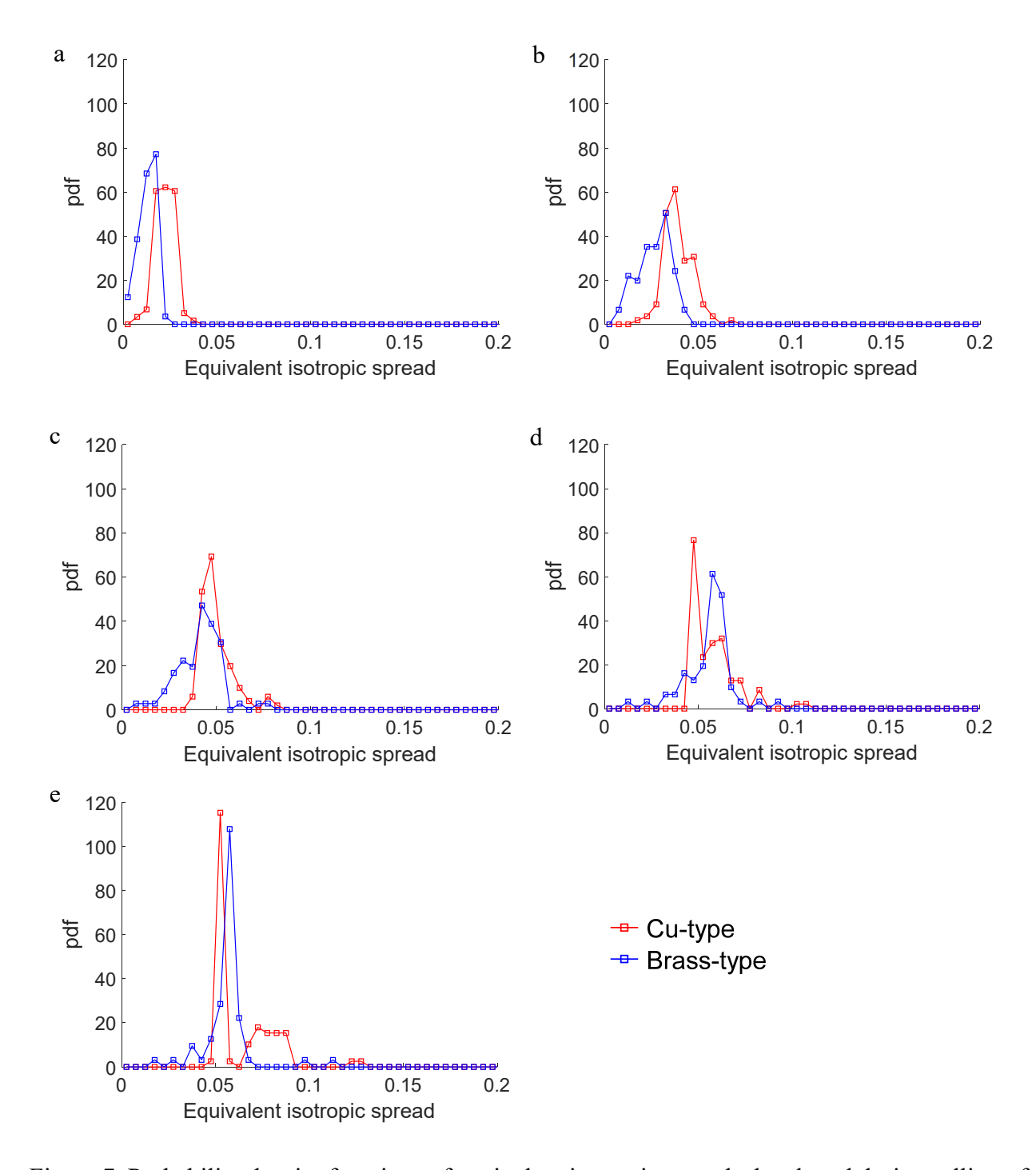


Figure 7. Probability density functions of equivalent isotropic spreads developed during rolling of Cu-type and brass-type textures predicted by FF-VPSC with plastic strain (a) 20% (0.22), (b) 40% (0.51), (c) 60% (0.92), (d) 80% (1.61), and (e) 95% ($\varepsilon_{VM} = 3.0$) reduction (true strain), respectively. For reference, the equivalent isotropic spread axes correspond to the misorientation angles as follows: $0.05=9.1^{\circ}$, $0.1=18.3^{\circ}$, $0.15=27.5^{\circ}$, $0.2=36.7^{\circ}$.

3.2 Deformed and recrystallized texture evolution in AA5182-O: Experiment and simulation

As a next case study, the simulations of deformation in simple tension and subsequent recrystallization were performed for an aluminum alloy, AA5182-O, using the FF-VPSC model. A velocity gradient, **L**, to impose the tension in the model is

$$\mathbf{L} = \begin{bmatrix} 1 & 0 & 0 \\ 0 & -0.5 & 0 \\ 0 & 0 & -0.5 \end{bmatrix} \tag{68}$$

A time increment is selected to provide a strain increment, $\Delta \varepsilon$, of 0.01. The initial texture of the alloy was measured using electron backscattered diffraction (EBSD) and represented using 1488 weighted grains. The grains deform by the FCC octahedral slip system $\{111\}\langle 1\bar{1}0\rangle$ [106-108] and with the linear hardening. The alloy was pulled in tension along the rolling direction (RD) using a continuous bending under tension (CBT) setup [109-115] to a greater strain level than achievable in tension. Fig. 8 shows IPF maps of the alloy in its as-received state and deformed in CBT to a tensile strain of 0.45. The figure also shows the corresponding grain average misorientation (GAM) maps. The measurement of the deformed structure allowed us to obtain a normalized distributions of GAM spreads, as shown in Fig. 9a. Pole figures showing the initial texture and the texture after CBT are shown in Fig. 10a and b, respectively. Fig. 10c shows the measured texture of the annealed alloy at 280° C for 2 hours. The recrystallized texture does not appear substantially different from the deformed texture but is much less intense than the deformed one.

Before showing simulated texture evolution, we show in Fig. 9b the calculated average intragranular misorientation spreads using the expression for obtaining a misorientation angle corresponding to a second moment of misorientation per grain r, $2\sqrt{\mathbf{I}:\langle\delta\mathbf{r}\otimes\delta\mathbf{r}\rangle^{(r)}}$, for all grains (all sub grains are considered separately) after deformation at a strain level of 0.45. A similar plot was obtained based on a set of discrete orientations selected from the misorientation spread per grain from which an average misorientation is calculated per grain.

The simulated texture after simple tension along RD to a strain of 0.45 is shown in Fig. 10b'. As expected, the texture evolution is such that the {111} peak arises along the pulling direction, RD, [116, 117]. Measured and simulated deformation textures have some differences because CBT is not exactly simple tension [118-121]. However, without relying on CBT, we would not be able to pull the alloy to such large strain necessary to promote texture evolution.

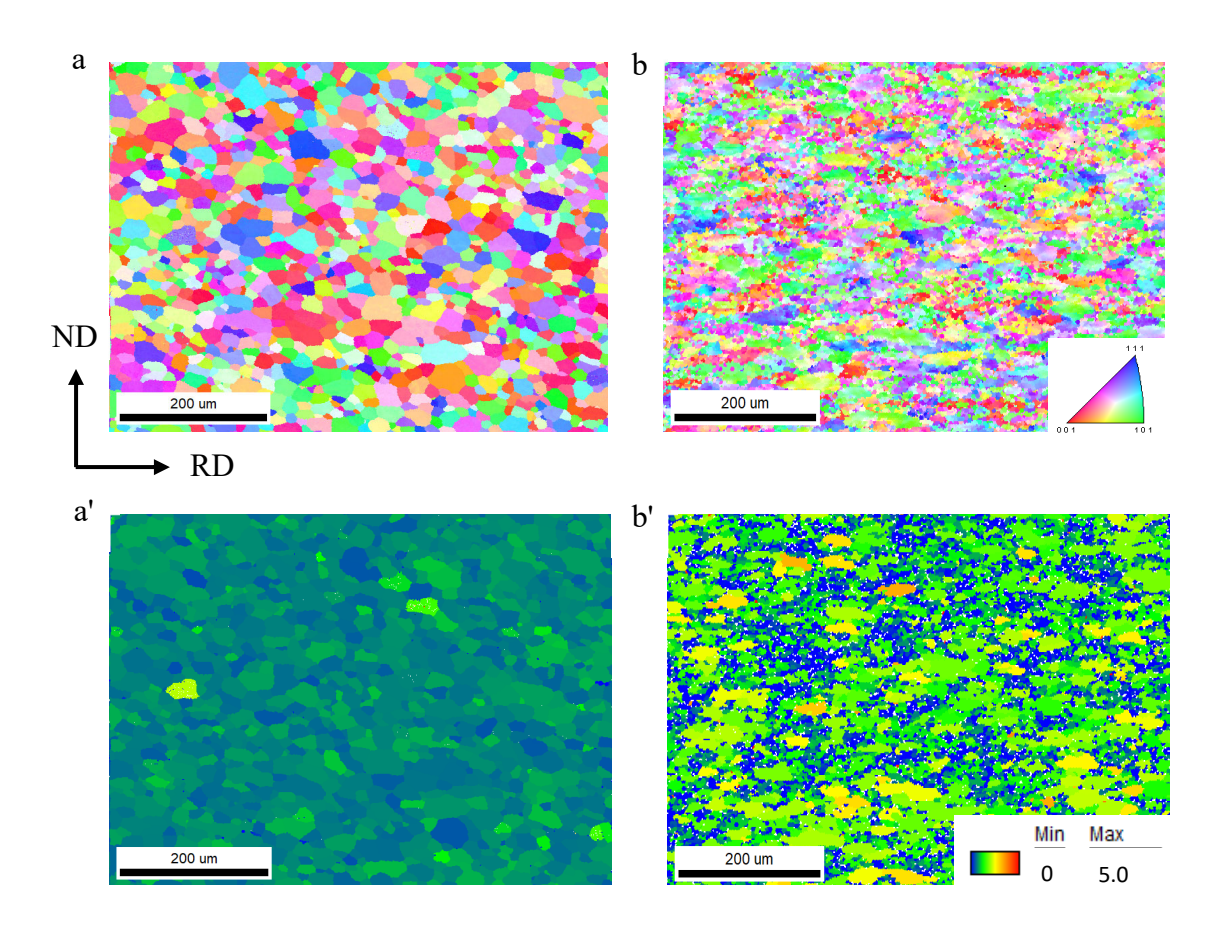
The simulated fully recrystallized texture is shown in Fig. 10c'. The parameters are given in Table 1. It is experimentally observed that the nucleation in aluminum alloys happens at grain boundaries [122-125]. The model was set such that the nucleation at grain boundaries is operative. A small percentage of transition bands (or bi-modal distribution) was predicted after the deformation simulation. The fraction was low given the relatively low strain level of deformation.

To quantify the texture differences, we calculate the pole figure difference[†] (PFD) between measured and predicted pole figures, which is given by [10, 126]:

$$PFD^{hkl} = \frac{\int_{\phi=0}^{2\pi} \int_{\theta=0}^{\pi/2} |I_{(\phi,\theta)}^{ref} - I_{(\phi,\theta)}| \sin\theta d\theta d\phi}{\int_{\phi=0}^{2\pi} \int_{\theta=0}^{\pi/2} |I_{(\phi,\theta)}^{ref} + I_{(\phi,\theta)}| \sin\theta d\theta d\phi},$$
(69)

where ϕ and θ are the longitude and latitude positions in an $\{hkl\}$ pole figure and $I_{(\phi,\theta)}^{ref}$ (corresponding to a reference taken to be measured texture) and $I_{(\phi,\theta)}$ (corresponding to predicted texture) are intensities. A value of PFD = 0 corresponds to a perfect match between the measured and the predicted pole figures and PFD = 1 corresponds to a perfect mismatch. Two textures with a PFD < 0.2 are considered to be in good agreement, and PFD < 0.1 represents excellent agreement. PFD between Fig. 10c and Fig. 10c' averaged over the poles is 0.13.

Results corresponding to Fig. 10b' and Fig. 10c' after proper modeling of hardening instead of the linear hardening are shown in appendix D.



[†] The pole figure difference indices were calculated using POLE ver. 8c, code developed by C.N. Tomé.

Figure 8. IPF maps showing grain structure in specimens of AA5182-O: (a) as-received and (b) deformed in CBT to a tensile strain of 0.45. Corresponding grain average misorientation (GAM) maps: (a') as-received and (b') deformed in CBT to a tensile strain of 0.45.

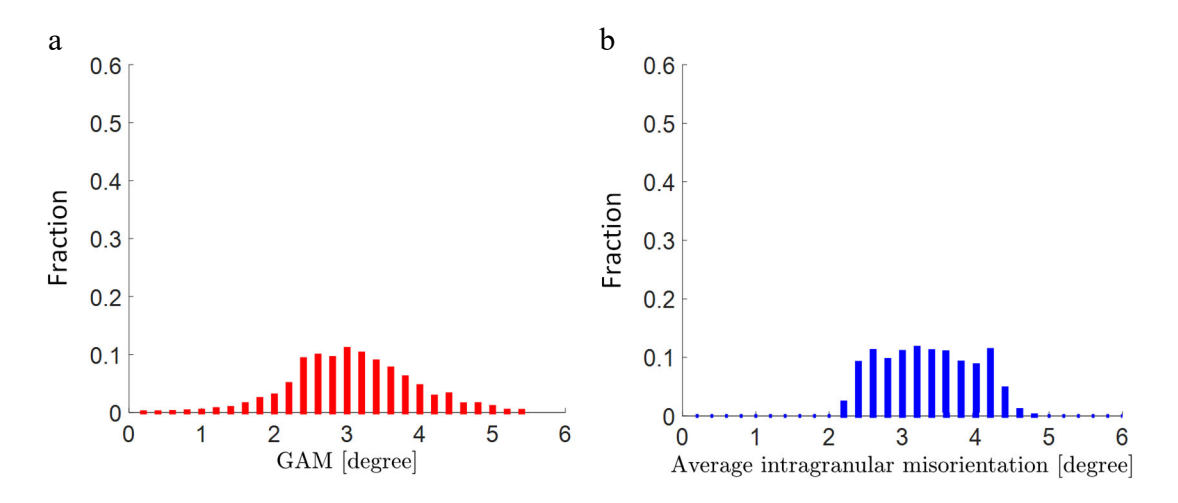


Figure 9. Normalized distributions showing (a) measured GAM spreads after CBT to a tensile strain of 0.45 and (b) corresponding simulated average intragranular misorientation spreads.

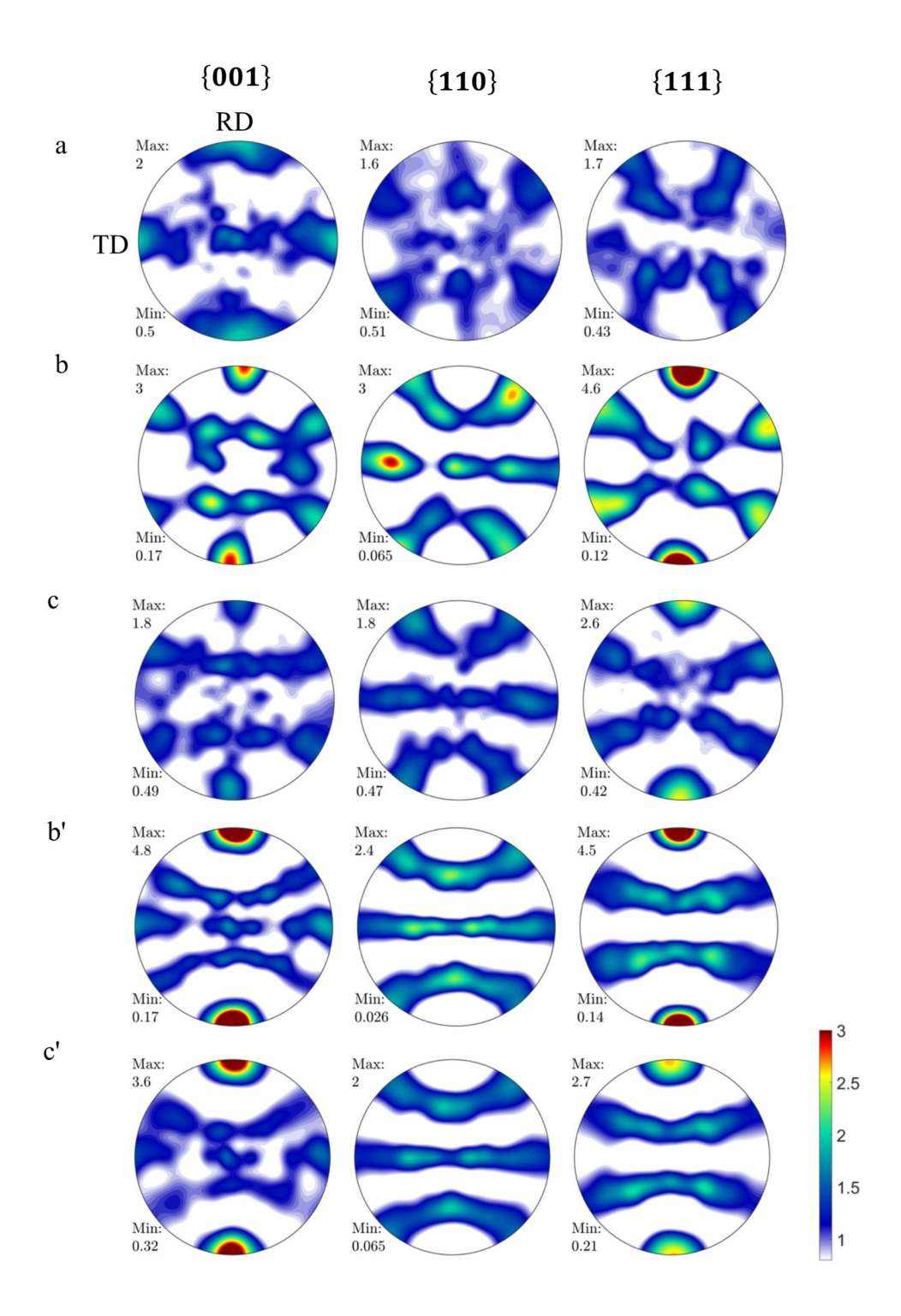


Figure 10. Pole figures of AA5182-O alloy: (a) measured initial texture in an as-received rolled and recrystallized specimen, (b) measured texture after CBT along RD of the as-received sheet to 0.45 tensile deformation, (c) measured texture after CBT followed by recrystallization, (b') predicted texture in tension along RD to a true strain of 0.45, and (c') predicted texture after tension followed by recrystallization.

3.3 Evolution of texture during recrystallization of MarM-509 alloy

Next, we present the simulations of texture evolution during recrystallization of a cobalt-based alloy, MarM-509, made by additively manufactured (AM) [127, 128]. The texture evolution of the alloy was measured using neutron diffractions (NeD). Fig. 11a shows pole figures of the measured initial texture. Pole figures showing texture used in the simulations were indistinguishable and are not shown. The measured initial texture was represented using 400 equally weighted crystal orientations. The initial texture used in the simulations was constructed from the measured using the procedure described in [129-132]. After AM, the alloy was annealed for 2, 6, and 10 hours at 2300 °F [127]. Figs. 11b, c, and d show measured recrystallization textures after for 2 hours (46% recrystallized), 6 hours (57% recrystallized), and 10 hours (91% recrystallized), respectively [127, 133].

Given that texture evolution was measured using NeD [134-138], orientation gradients in grains were zero. However, the AM process produces grains with some orientation spread. For simulations of recrystallization, it was necessary to create some spreads in grains for nucleation and to induce some stored energy for nucleation and growth. In our recrystallization model, the nucleation of grains is driven by the strain energy and gradient in orientation, where the orientation gradients depend on the intragranular orientation spreads, $\langle \delta \mathbf{r} \otimes \delta \mathbf{r} \rangle^{(r)}$. The nucleation was modeled using the grain boundary nucleation model. The alloy was deformed in compression along RD to a strain of 0.1 by $\{111\}\langle 1\bar{1}0 \rangle$ FCC octahedral slip systems with linear hardening. Lower strain levels were insufficient for recrystallization, while higher levels like 0.15 or 0.2 produced similar results like those at 0.1 pre-strain.

The predicted recrystallization textures for 46%, 57%, 91% recrystallized structure are shown in Figs. 11b', c', and d', respectively. These simulated recrystallized textures show good agreement with the measured textures and can capture all components in the pole figures. In the simulations, percentage of recrystallization is regulated by the time increment Δt used in Eq. 61 and Eq. 62 and the number of increments. Larger values of Δt results in more nucleated grains leading to higher percentage of recrystallization and Δt is the fitting parameter to get desired percentage of recrystallization. The parameters are given in Table 1. PFDs between Fig. 11b and Fig. 11b', Fig. 11c and Fig. 11c', and Fig. 11d and Fig. 11d' are 0.06, 0.08, and 0.09, respectively.

While it is observed that the application of the compressive strain energy lead to the recrystallization textures that match well the measured recrystallized textures, we would like to indicate that pre-deformation in tension did not yield such good prediction suggesting that misorientation trends after AM were more similar to those induced using compression along RD than tension.

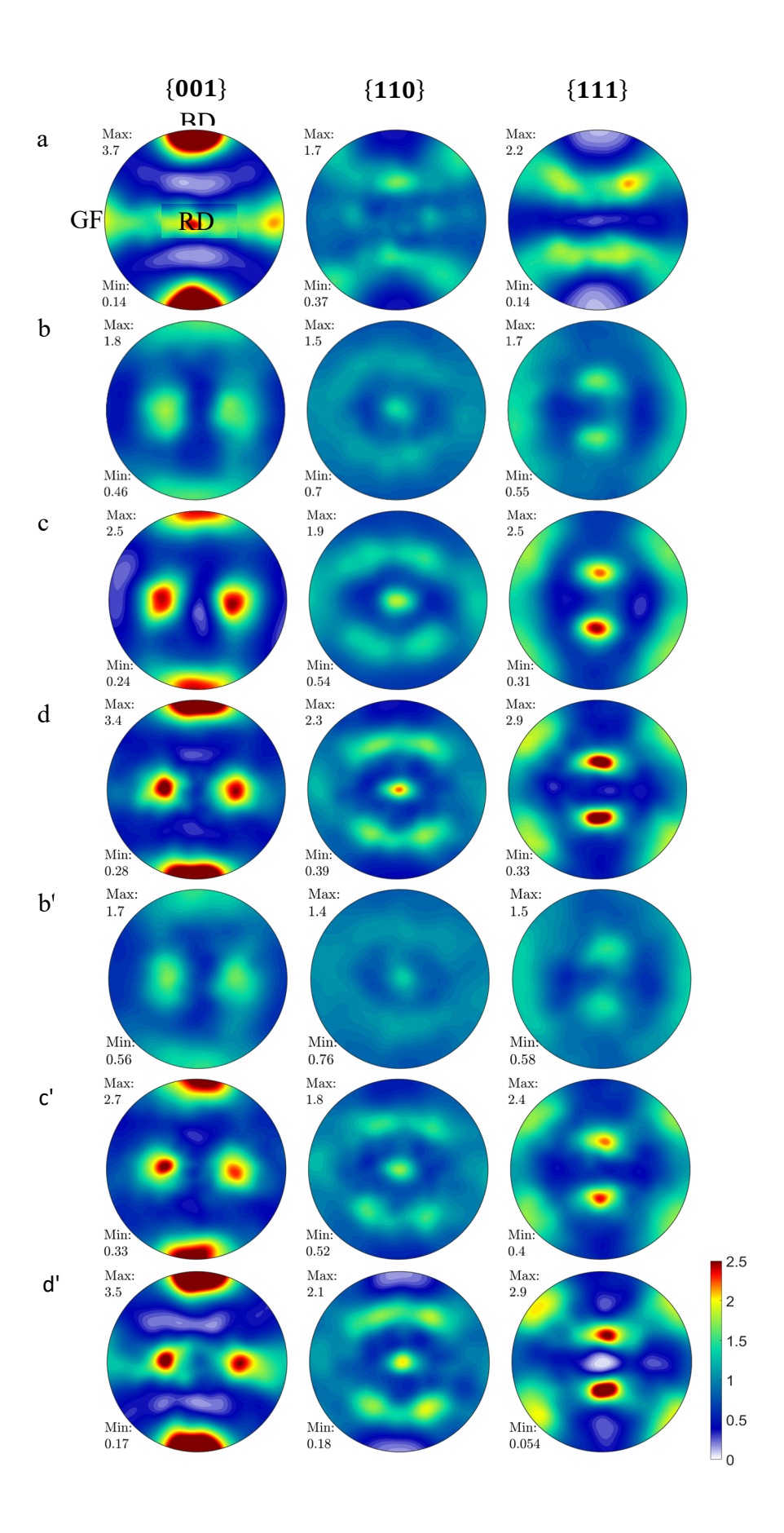


Figure 11. Pole figures showing texture evolution during annealing of MarM-509 alloy at 2300 °F: (a) measured initial texture in an as-built specimen, (b) measured texture in a specimen after annealing for 2 hours, (c) measured texture in a specimen after annealing for 6 hours, (d) measured texture in a specimen after annealing for 10 hours, (b') predicted recrystallization texture corresponding to (b), (c') predicted recrystallization texture corresponding to (c) and (d') predicted recrystallization texture corresponding to (d). The additive manufacturing specimen frame is defined as build direction (BD), recoat direction (RD), and gas flow direction (GF).

3.4 Deformed and recrystallized textures of interstitial free (IF) steel

Finally, the simulations of texture evolution of Ti-Nb IF steel to 85% rolling reduction and subsequent recrystallization are performed and compared to experimental results [139, 140]. For these simulations, the BCC metal is represented with 400 randomly oriented spherical grains deforming by {110}(111) and {112}(111) slip systems with the linear hardening under Eq. (67) boundary conditions.

Fig. 12a shows the $\varphi_2 = 45^\circ$ section of Euler space for the measured rolling texture [139, 140], while Fig. 12a' shows the predicted deformed texture. Majority of the orientations concentrate around the γ -fiber and a portion of the α -fiber [141-143]. A figure in Appendix A shows α and γ fibers. Fig. 12b and Fig. 12b' show the $\varphi_2 = 45^\circ$ section of Euler space for the measured and predicted recrystallization textures. Comparing measured recrystallized texture with measured deformed texture, it is evident that γ -fiber strength increases during recrystallization while α -fiber weakens [141, 143-146]. The grains on γ -fiber have higher stored energy and are favorable nucleation sites [145, 147-149] during recrystallization. It is also observed that nuclei grow around the grain boundaries [140, 150]. In the simulation, the grain boundary nucleation was operative. The parameters are given in Table 1.

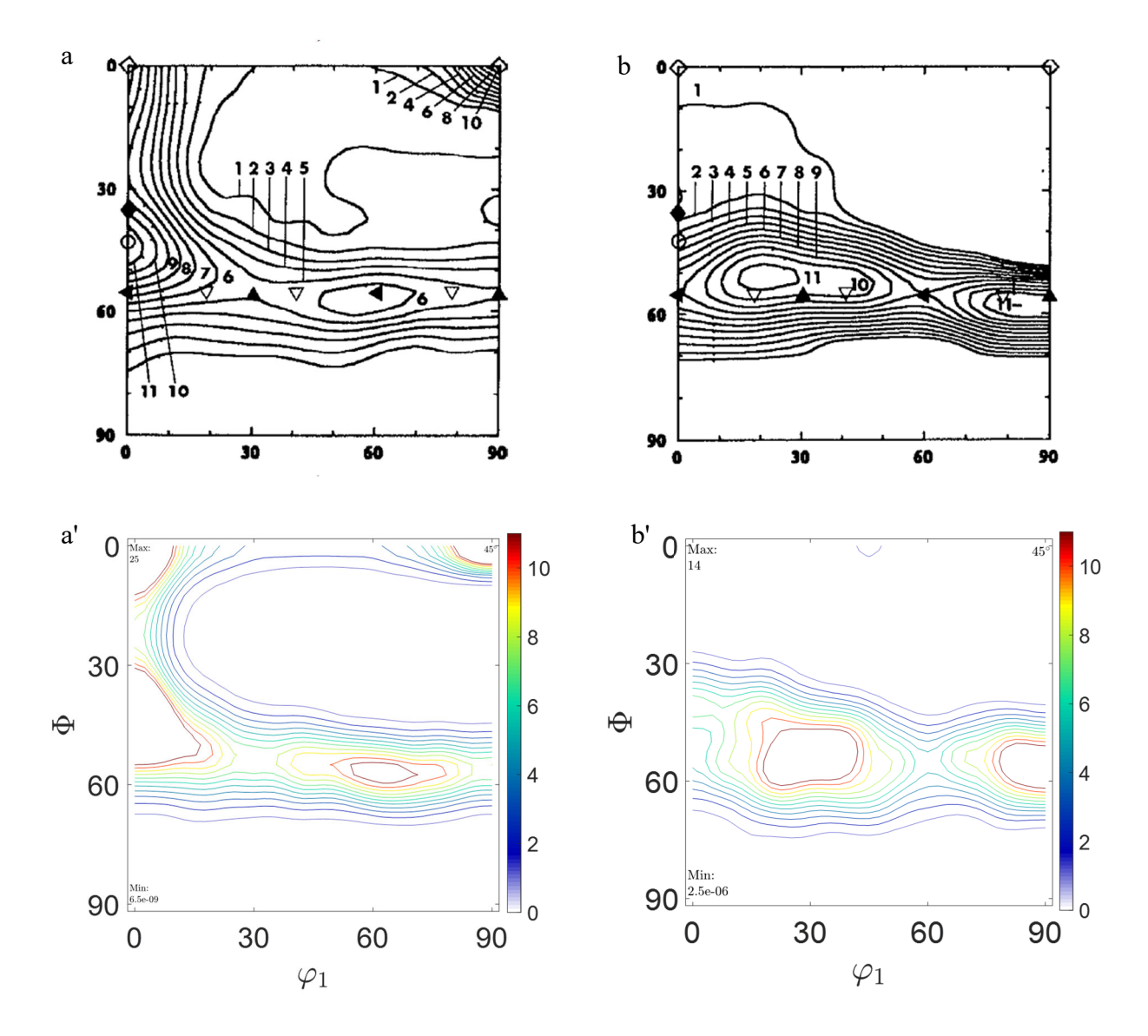


Figure 12. ODF sections at $\varphi_2 = 45^\circ$ showing (a) measured deformation texture in interstitial-free (IF) steel rolled to 85% reduction, (b) measured recrystallization texture after rolling, (a') predicted deformed texture, and (b') predicted recrystallized texture.

Table 1. Recrystallization model parameters per material. The identification of the parameters was accomplished as follows: first, $\delta\theta_{th}$ and E_{th} are set to nearly zero or zero to promote the probability to nucleate new grains during recrystallization, next, the parameters A and B are adjusted to obtain an appropriate rate of nucleation, and finally, M is adjusted to obtain % recrystallized structure per simulation case. Also, the parameters are chosen to promote a desired type of nucleation. For example, to promote the TB nucleation, the parameters A_{tb} and B_{tb} must be set to lower values than A_{gb} and B_{gb} . While automated methodologies for parameter identification exist in the literature [151, 152], a manual procedure was employed in the present

work. Δt is also a fitting parameter to get a desired % of recrystallization. Larger values of Δt results in more nucleated grains leading to higher % of recrystallized structure.

		Cu-type	Brass-type	AA5182-O	IF-steel	MarM-509
Grain boundary nucleation	E_{th}^{gb}	0.0	0.0	0.0	0.0	0.0
	$\delta heta_{th}^{gb}$	1.2	1.2	1.5×10^{-3}	1.1	1.5×10^{-3}
	A_{gb}	5.21×10^5	2.15×10^{3}	3.5×10^{-4}	1.55×10^{5}	1.5×10^{-5}
	B_{gb}	3.06×10^{-6}	3.1×10^{-6}	3.5×10^{-7}	3.5×10^{-7}	3.5×10^{-7}
	С	2.0	2.0	2.0	2.0	2.0
Transition band nucleation	E_{th}^{tb}	0.0	0.0	0.0	N/A	N/A
	$\delta heta_{th}^{tb}$	0.9	0.1	N/A	N/A	N/A
	A_{tb}	5.21×10^{5}	2.15×10^{2}	N/A	N/A	N/A
	B_{tb}	3.06×10^{-6}	3.1×10^{-6}	N/A	N/A	N/A
Growth	М	3.0×10^{-9}	3.0×10^{-9}	1.5×10^{-9}	3.0×10^{-9}	1.5×10^{-5}
Time increment	Δt	0.2	0.2	0.2	0.2	0.0015 (46%) 0.0036 (57%) 0.02 (92%)

4. Conclusions

In this work, we integrated a deformation model considering fragmentation of grains and a recrystallization model formulated based on intragranular orientation distributions and strain energy fields into a computationally efficient mean-field model termed FF-VPSC. The FF-VPSC model predicted both a Cu-like texture formation in a high SFE metal and a brass-like texture formation in a low SFE metal after rolling to very large plastic strains to agree well with experimental measurements. While the former texture evolution was successfully predicted using several mean-field crystal plasticity models, the available mean-field models were challenged greatly at predicting the latter texture evolution. We have shown that a combination of not only including deformation twinning but also accounting for orientation gradients along with grain fragmentation facilitated predicting the brass-like texture evolution in low SFE metals. Subsequently, the recrystallization texture evolution for the two texture types was simulated and good agreements with corresponding experiments were achieved. Three additional case studies were run to demonstrate effectiveness of the model in predicting effects of strain-path, stored energy, and crystal structure on the predictions. To this end, tension and recrystallization of an aluminum alloy 5182-O, recrystallization of an AM cobalt-based alloy MarM-509 and rolling and recrystallization of an IF steel were simulated to predict texture evolution. Comparisons with

experiments revealed good predictions for all these simulation cases. We found that tradeoffs between transition-bands and grain boundary nucleation mechanisms enabled such good predictions of the recrystallization texture evolution. The nucleation mechanisms were driven by the misorientation spreads in grains, the former by the bi-modal spreads and underlying transition bands, while the latter by the unimodal spreads. To achieve good predictions of the recrystallization texture evolution, the Cu-type and brass-type rolled textures underwent the transition band nucleation, while AA, MarM509, and IF steel underwent the grain boundary nucleation. The work confirmed that the consideration of intragranular misorientation fluctuations and grain fragmentations is essential for predicting texture evolution during deformation and recrystallization.

Acknowledgements

This research was sponsored by the U.S. National Science Foundation and was accomplished under the Grant No. OIA-1757371. The authors also acknowledge discussions and input from Drs. Miroslav Zecevic and João Fonseca.

Appendix A

This appendix depicts FCC texture components in Fig. A1 and BCC texture fibers in Fig. A2. It also shows the VPFFT model in Fig. A3.

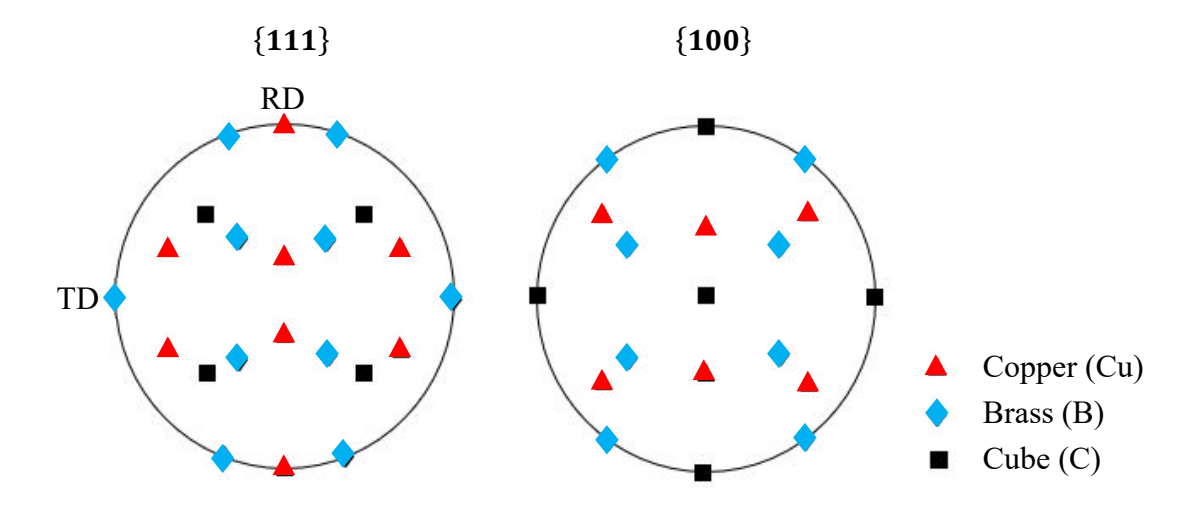


Figure A1. {111} and {100} pole figures showing the rolling and recrystallization texture components for FCC metals: copper, brass, and cube.

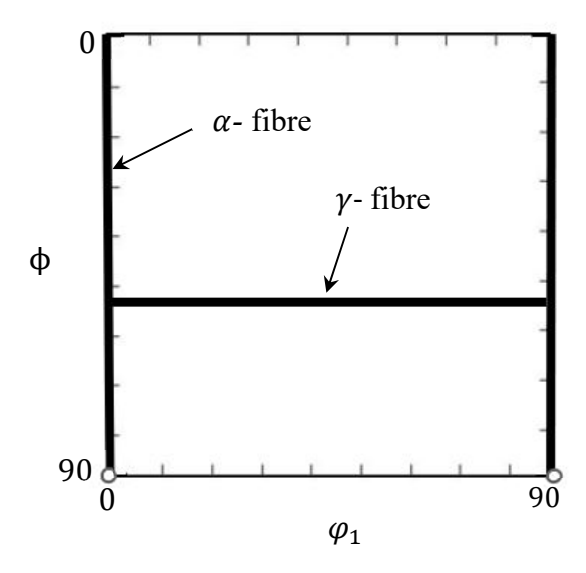


Figure A2. An ODF section at $\varphi_2 = 45^{\circ}$ showing α and γ fibers for BCC metals.

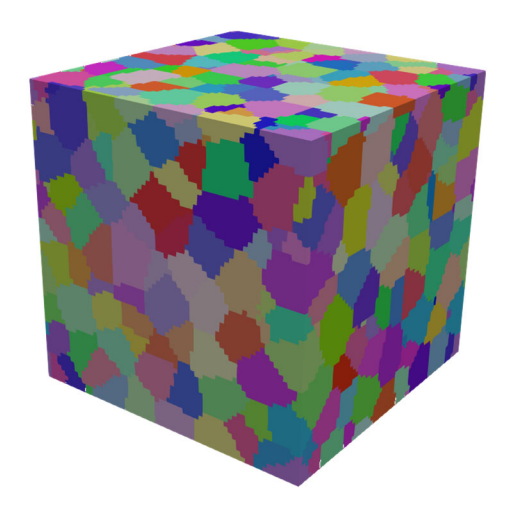


Figure A3. Voxel-based (128³) microstructural cell consisting of 400 grains used for the VPFFT simulations.

Appendix B

The linear mapping of stress fluctuations from time $t - \Delta t$ to t caused by spatial variation of mean stress values is performed by a linear mapping matrix $\mathbf{Z}^{(r)}$. At time $t - \Delta t$ (the first step of deformation), the second moment of stress without any spatial mean stress effect and misorientation effect is calculated using the RHS term of Eq. (20) as:

$$\langle \mathbf{\sigma}^{t-\Delta t} \otimes \mathbf{\sigma}^{t-\Delta t} \rangle^{(r)} = \frac{2}{w^{t-\Delta t(r)}} \frac{\partial \widetilde{U}_{T}^{t-\Delta t}}{\partial \mathbf{M}^{t-\Delta t(r)}}$$
(B1)

Eq. (20) at the time step $t - \Delta t$ is:

$$\langle \mathbf{\sigma}^{t-\Delta t} \otimes \mathbf{\sigma}^{t-\Delta t} \rangle^{(r)} = \mathbf{\sigma}^{t-\Delta t(r)} \otimes \mathbf{\sigma}^{t-\Delta t(r)} + \langle \delta \mathbf{\sigma}^{t-\Delta t(\bar{q})} \otimes \delta \mathbf{\sigma}^{t-\Delta t(\bar{q})} \rangle^{(r)}$$
(B2)

Rearranging Eq. (B2) we get the expression for the second moment of stress fluctuations influenced by the variation of the spatial mean value as the difference of the second and first moment of stress field calculated at the first deformation step as:

$$\langle \delta \mathbf{\sigma}^{t-\Delta t(\bar{q})} \otimes \delta \mathbf{\sigma}^{t-\Delta t(\bar{q})} \rangle^{(r)} = \langle \mathbf{\sigma}^{t-\Delta t} \otimes \mathbf{\sigma}^{t-\Delta t} \rangle^{(r)} - \mathbf{\sigma}^{t-\Delta t(r)} \otimes \mathbf{\sigma}^{t-\Delta t(r)}$$
(B3)

Now, the calculation of the mapping matrix $\mathbf{Z}^{(r)}$ is described:

The term $\langle \delta \sigma^{t-\Delta t(\bar{q})} \otimes \delta \sigma^{t-\Delta t(\bar{q})} \rangle^{(r)}$ is decomposed into a lower triangular matrix $\mathbf{L}^{t-\Delta t}$ and its conjugate transpose by Cholesky decomposition.

At the second deformation step i.e., at the time t, we calculate the second moment of stress without fluctuations of mean stress value and misorientation effects as:

$$\langle \mathbf{\sigma}^t \otimes \mathbf{\sigma}^t \rangle^{(r)} = \frac{2}{w^{t(r)}} \frac{\partial \tilde{U}_T^t}{\partial \mathbf{M}^{t(r)}}$$
(B4)

Now, by subtracting the first moment from the second moment we get an expression like the RHS of Eq. (B3) expressed as: $\langle \boldsymbol{\sigma}^t \otimes \boldsymbol{\sigma}^t \rangle^{(r)} - \boldsymbol{\sigma}^{t(r)} \otimes \boldsymbol{\sigma}^{t(r)}$. This term is then decomposed into a lower triangular term \mathbf{L}^t and its conjugate transpose.

We can now write mapping of \mathbf{L}^t as a composition of mapping of $\mathbf{L}^{t-\Delta t}$ and mapping matrix $\mathbf{Z}^{(r)}$ as

 $\mathbf{L}^t = \mathbf{Z}^{(r)} \mathbf{L}^{t-\Delta t}$ which can also be written as:

$$\mathbf{Z}^{(r)} = \mathbf{L}^t (\mathbf{L}^{t-\Delta t})^{-1} \tag{B5}$$

Finally, the second moment of stress due to the mean stress fluctuations at time t is mapped using the matrix $\mathbf{Z}^{(r)}$ as:

$$\langle \delta \boldsymbol{\sigma}^{t(\bar{q})} \otimes \delta \boldsymbol{\sigma}^{t(\bar{q})} \rangle^{(r)} = \mathbf{Z}^{(r)} \langle \delta \boldsymbol{\sigma}^{t-\Delta t(\bar{q})} \otimes \delta \boldsymbol{\sigma}^{t-\Delta t(\bar{q})} \rangle^{(r)} (\mathbf{Z}^{(r)})^T$$
(B6)

where $(\mathbf{Z}^{(r)})^{\mathrm{T}}$ is transpose of $\mathbf{Z}^{(r)}$.

Appendix C

As explained in the text, the cross-correlation term in Eq. (27), $\langle \delta \boldsymbol{\sigma}^{t(\bar{q})} \otimes \delta \boldsymbol{\sigma}^{t(\delta r)} \rangle^{(r)}$, is approximated using a cross-covariance term, $\langle \delta \boldsymbol{\sigma}^{t(\bar{q})} \otimes \delta \mathbf{r}^t \rangle^{(r)}$, arising due to the stress fluctuations caused by mean grain properties and misorientation fluctuations inside a grain as:

$$\langle \delta \boldsymbol{\sigma}^{t(\bar{q})} \otimes \delta \boldsymbol{\sigma}^{t(\delta r)} \rangle^{(r)} = \langle \delta \boldsymbol{\sigma}^{t(\bar{q})} \otimes \delta \mathbf{r}^{t} \rangle^{(r)} \left(\frac{\partial \boldsymbol{\sigma}}{\partial \delta \mathbf{r}} \Big|_{\boldsymbol{\sigma}^{(r)}, \bar{\mathbf{q}}^{(r)}}^{t} \right)^{T}, \tag{C1}$$

where $\frac{\partial \mathbf{\sigma}}{\partial \delta \mathbf{r}}$ is a derivative of Eq. (3) considering $\dot{\mathbf{\epsilon}}$ as a constant: $\frac{\partial \mathbf{\epsilon}}{\partial \delta \mathbf{r}} = \mathbf{m}^{s} \left(\dot{\gamma}_{0} \sum_{s} n \left(\frac{|\mathbf{\sigma}:\mathbf{m}^{s}|}{\tau_{c}^{s}} \right)^{n-1} \frac{\partial}{\partial \delta \mathbf{r}} \left(\frac{|\mathbf{\sigma}:\mathbf{m}^{s}|}{\tau_{c}^{s}} \right) \right) + \dot{\gamma}_{0} \sum_{s} \left(\frac{|\mathbf{\sigma}:\mathbf{m}^{s}|}{\tau_{c}^{s}} \right)^{n} \frac{\partial \mathbf{m}^{s}}{\partial \delta \mathbf{r}}$ yielding:

$$\frac{\partial \mathbf{\sigma}}{\partial \delta \mathbf{r}} = -\left[\sum_{s} \mathbf{m}^{s} \otimes \frac{\partial \dot{\gamma}^{s}}{\partial \mathbf{\sigma}}\right]^{-1} \left\{\sum_{s} \left[\mathbf{m}^{s} \otimes \left(\frac{\partial \dot{\gamma}^{s}}{\partial \mathbf{m}^{s}} \frac{\partial \mathbf{m}^{s}}{\partial \delta \mathbf{r}}\right) + \dot{\gamma}^{s} \frac{\partial \mathbf{m}^{s}}{\partial \delta \mathbf{r}}\right]\right\},\tag{C2}$$

where $\frac{\partial \dot{\gamma}^s}{\partial \sigma} = \dot{\gamma}_0 n \left(\frac{|\sigma: \mathbf{m}^s|}{\tau_c^s}\right)^{n-1} \mathbf{m}^s \frac{1}{\tau_c^s}$, and $\frac{\partial \dot{\gamma}^s}{\partial \mathbf{m}^s} = \dot{\gamma}_0 n \left(\frac{|\sigma: \mathbf{m}^s|}{\tau_c^s}\right)^{n-1} \mathbf{\sigma} \frac{1}{\tau_c^s}$ are obtained by taking the derivatives of Eq. (2). Finally, $\frac{\partial \mathbf{m}^s}{\partial \delta \mathbf{r}}$ is simply evaluated using $\frac{\partial \mathbf{m}^s}{\partial \delta \mathbf{r}} = \frac{\partial \mathbf{m}^s}{\partial \delta \mathbf{R}} \frac{\partial \delta \mathbf{R}}{\partial \delta \mathbf{r}}$, where $\delta \mathbf{R}$ is the rotation matrix representation of the rotation of misorientation vector $\delta \mathbf{r}$.

The cross-covariance term, $\langle \delta \boldsymbol{\sigma}^{t(\bar{q})} \otimes \delta \mathbf{r}^t \rangle^{(r)}$, owing to the fluctuations of mean grain properties $\delta \boldsymbol{\sigma}^{t(\bar{q})}$ and misorientation fluctuations $\delta \mathbf{r}^t$ at a time t is obtained by a linear mapping matrix $\mathbf{Z}^{(r)}$ (described in Appendix B) given the cross-covariance term $\langle \delta \boldsymbol{\sigma}^{t-\Delta t(\bar{q})} \otimes \delta \mathbf{r}^{t-\Delta t} \rangle^{(r)}$ at time $t-\Delta t$ is known. Assuming a linear relationship between stress fluctuations due to mean grain properties from time $t-\Delta t$ to t, the mapping is:

$$\delta \mathbf{\sigma}^{t(\bar{q})}(\mathbf{x}) = \mathbf{Z}^{(r)} \delta \mathbf{\sigma}^{t-\Delta t(\bar{q})}. \tag{C4}$$

The misorientation $\delta \mathbf{r}^t$ at t can be approximated as the function of $\delta \boldsymbol{\sigma}^{t-\Delta t(\bar{q})}$ and $\delta \mathbf{r}^{t-\Delta t}$ after utilizing Eqs. ((29), (43)) and substituting $\delta \mathbf{r}^{t,rot}(\mathbf{x}) = \overline{\mathbf{R}}_{inc}^{t,(r)} \delta \mathbf{r}^t(\mathbf{x})$ and $\delta \mathbf{r}_{inc}^t = \delta \dot{\boldsymbol{\omega}}^t(\mathbf{x})$ as:

$$\delta \mathbf{r}^{t}(\mathbf{x}) = \mathbf{Y}^{(\delta r)(r)} \delta \mathbf{r}^{t-\Delta t}(\mathbf{x}) + \mathbf{Y}^{(\delta \sigma)(r)} \delta \mathbf{\sigma}^{t-\Delta t(\bar{q})}(\mathbf{x}), \tag{C5}$$

$$\mathbf{Y}^{(\delta\sigma)(r)} = \frac{\Delta t}{2} \frac{\partial \dot{\mathbf{\omega}}}{\partial \sigma} \Big|_{\mathbf{\sigma}^{(r)}, \overline{\mathbf{q}}^{(r)}}^{t-\Delta t}, \tag{C6}$$

$$\mathbf{Y}^{(\delta r)(r)} = \frac{\Delta t}{2} \frac{\partial \dot{\mathbf{\omega}}}{\partial \sigma} \Big|_{\boldsymbol{\sigma}^{(r)}, \overline{\mathbf{q}}^{(r)}}^{t - \Delta t} \frac{\partial \sigma}{\partial \delta r} \Big|_{\boldsymbol{\sigma}^{(r)}, \overline{\mathbf{q}}^{(r)}}^{t - \Delta t} + \frac{\Delta t}{2} \frac{\partial \dot{\mathbf{\omega}}}{\partial \delta r} \Big|_{\boldsymbol{\sigma}^{(r)}, \overline{\mathbf{q}}^{(r)}}^{t - \Delta t} + \overline{\mathbf{R}}_{inc}^{t - \Delta t, (r)}. \tag{C7}$$

The derivative terms in Eqs. ((C6), and (C7)) are calculated as follows (note these are used in Eq. (31)):

$$\frac{\partial \dot{\omega}}{\partial \sigma} = -\frac{\partial \dot{\omega}^p}{\partial \sigma} = -\sum_s \alpha^s \otimes \frac{\partial \dot{\gamma}^s}{\partial \sigma},\tag{C8a}$$

$$\frac{\partial \dot{\omega}}{\partial \delta \mathbf{r}} = -\frac{\partial \dot{\omega}^p}{\partial \delta \mathbf{r}} = -\sum_{s} \left[\boldsymbol{\alpha}^s \otimes \left(\frac{\partial \dot{\gamma}^s}{\partial \mathbf{m}^s} \frac{\partial \mathbf{m}^s}{\partial \delta \mathbf{r}} \right) + \dot{\gamma}^s \frac{\partial \boldsymbol{\alpha}^s}{\partial \delta \mathbf{r}} \right]. \tag{C8b}$$

Using Eqs. ((C4), and (C5)), the term $\langle \delta \sigma^{t(\bar{q})} \otimes \delta \mathbf{r}^t \rangle^{(r)}$ is calculated as:

$$\langle \delta \mathbf{\sigma}^{t(\bar{q})} \otimes \delta \mathbf{r}^{t} \rangle^{(r)} = \mathbf{Z}^{(r)} \langle \delta \mathbf{\sigma}^{t-\Delta t(\bar{q})} \otimes \delta \mathbf{r}^{t-\Delta t} \rangle^{(r)} \mathbf{Y}^{(\delta r)(r)^{T}} + \mathbf{Z}^{(r)} \langle \delta \mathbf{\sigma}^{t-\Delta t(\bar{q})} \otimes \delta \mathbf{\sigma}^{t-\Delta t(\bar{q})} \rangle^{(r)} \mathbf{Y}^{(\delta \sigma)(r)^{T}}.$$
(C9)

Also, at time $t - \Delta t$, the cross-covariance term $\langle \delta \mathbf{\sigma}^{t - \Delta t(\bar{q})} \otimes \delta \mathbf{r}^{t - \Delta t} \rangle^{(r)}$ is:

$$\langle \delta \mathbf{\sigma}^{t-\Delta t(\bar{q})} \otimes \delta \mathbf{r}^{t-\Delta t} \rangle^{(r)} = \mathbf{Z}^{(r)} \langle \delta \mathbf{\sigma}^{t-\Delta t(\bar{q})} \otimes \delta \mathbf{\sigma}^{t-\Delta t(\bar{q})} \rangle^{(r)} \mathbf{Y}^{(\delta \sigma)(r)^{T}}. \tag{C10}$$

The second moment of stress fluctuations because of intragranular misorientation fluctuations term in Eq. (27), $\langle \delta \sigma^{t(\delta r)} \otimes \delta \sigma^{t(\delta r)} \rangle^{(r)}$, can now be evaluated using:

$$\langle \delta \mathbf{\sigma}^{t(\delta r)} \otimes \delta \mathbf{\sigma}^{t(\delta r)} \rangle^{(r)} = \frac{\partial \mathbf{\sigma}}{\partial \delta \mathbf{r}} \Big|_{\mathbf{\sigma}^{(r)}, \overline{\mathbf{q}}^{(r)}}^{t} \langle \delta \mathbf{r}^{t} \otimes \delta \mathbf{r}^{t} \rangle^{(r)} \left(\frac{\partial \mathbf{\sigma}}{\partial \delta \mathbf{r}} \Big|_{\mathbf{\sigma}^{(r)}, \overline{\mathbf{q}}^{(r)}}^{t} \right)^{T}, \tag{C11}$$

where the second moment of misorientations term $\langle \delta \mathbf{r}^t \otimes \delta \mathbf{r}^t \rangle^{(r)}$ is expressed in Eq. (44).

Appendix D

This appendix shows that the simplifications introduced into the evolution of hardening per case study play a secondary role in the evolution of texture. Given that we do not have flow stress data for all materials, we fitted a tensile stress-strain response for AA5182-O with a dislocation density-based hardening law available in our model [153, 154] and then simulated the deformation and recrystallization texture evolution for the alloy. Hardening of cubic metals is usually assumed to be isotropic over slip systems per grain. The hardening varies from grain to grain but slip systems per grain harden equally. As a result, the activity of slip systems per grain is not influenced by hardening but by crystal orientation only. Therefore, texture evolution is not a strong function of the evolution of slip resistance. Fig. D2a and Fig. D2b are predicted after correct modeling of hardening. The results are like those in Fig. 10b' and Fig. 10c', which are based on the simplified hardening.

For completeness of the present work, we provide a brief summary of the dislocation density hardening law. To estimate the resistance required to trigger slip systems, s, from the octahedral family, α , we consider the contributions of the following terms: a friction stress $\tau_{0,f}^{\alpha}$, a forest dislocation interaction stress τ_{for}^{α} , and a dislocation substructure/debris interaction stress τ_{sub}^{α} :

$$\tau_c^{\alpha} = \tau_{0,f}^{\alpha} + \tau_{for}^{\alpha} + \tau_{sub}^{\alpha}. \tag{D1}$$

The individual values of τ_{for}^{α} and τ_{sub}^{α} are governed by the evolution of the dislocation densities, i.e. the forest ρ_{for}^{α} and substructure/debris ρ_{sub}^{α} dislocations, evolving from their initial values given in Table D1. Taylor-like laws are used to represent these relationships for each dislocation type:

$$\tau_{for}^{\alpha} = \chi b^{\alpha} \mu^{\alpha} \sqrt{\rho_{for}^{\alpha}},\tag{D2}$$

$$\tau_{sub}^{\alpha} = k_{sub} \mu^{\alpha} b^{\alpha} \sqrt{\rho_{sub}} log\left(\frac{1}{b^{\alpha} \sqrt{\rho_{sub}}}\right). \tag{D3}$$

Here χ is a dislocation interaction constant set to 0.9 and $k_{sub} = 0.086$ is a mathematical parameter that insures that Eq. (D2) compensates the Taylor law at low dislocation densities [155]. The value of the forest density ρ_{for}^{α} changes according to competition between the rate of storage/generation and the rate of dynamic recovery/removal as:

$$\frac{\partial \rho_{for}^{\alpha}}{\partial \gamma^{\alpha}} = \frac{\partial \rho_{gen,for}^{\alpha}}{\partial \gamma^{\alpha}} - \frac{\partial \rho_{rem,for}^{\alpha}}{\partial \gamma^{\alpha}} = k_1^{\alpha} \sqrt{\rho_{for}^{\alpha}} - k_2^{\alpha} (\dot{\varepsilon}, T) \rho_{for}^{\alpha}, \quad \Delta \rho_{for}^{\alpha} = \frac{\partial \rho_{for}^{\alpha}}{\partial \gamma^{\alpha}} |\Delta \gamma^{\alpha}|. \tag{D4}$$

In Eq. (D4), k_1^{α} is a coefficient for the rate of dislocation storage because of statistical trapping of gliding dislocations and k_2^{α} is the coefficient determining the rate of dynamic recovery by thermally activated mechanisms. The second coefficient is calculated using:

$$\frac{k_2^{\alpha}(\dot{\varepsilon},T)}{k_1^{\alpha}} = \frac{\chi b^{\alpha}}{g^{\alpha}} \left(1 - \frac{kT}{D^{\alpha}b^3} ln\left(\frac{\dot{\varepsilon}}{\dot{\varepsilon}_0}\right) \right), \tag{D5}$$

where k, $\dot{\varepsilon}_0$, g^{α} and D^{α} are respectively Boltzmann's constant, a reference strain rate (taken here to be 10^7 s⁻¹), an effective activation enthalpy and a drag stress. Lastly, the increment in substructure/debris development is related to the rate of dynamic recovery of all active dislocations as:

$$\Delta \rho_{sub} = \sum_{\alpha} q b^{\alpha} \frac{\partial \rho_{rem,for}^{\alpha}}{\partial \gamma^{\alpha}} |\Delta \gamma^{\alpha}|, \tag{D6}$$

where q is a rate parameter that determines the fraction of an α -type dislocations that do not annihilate, but become substructure dislocation. The parameters of the law are given in Table D1.

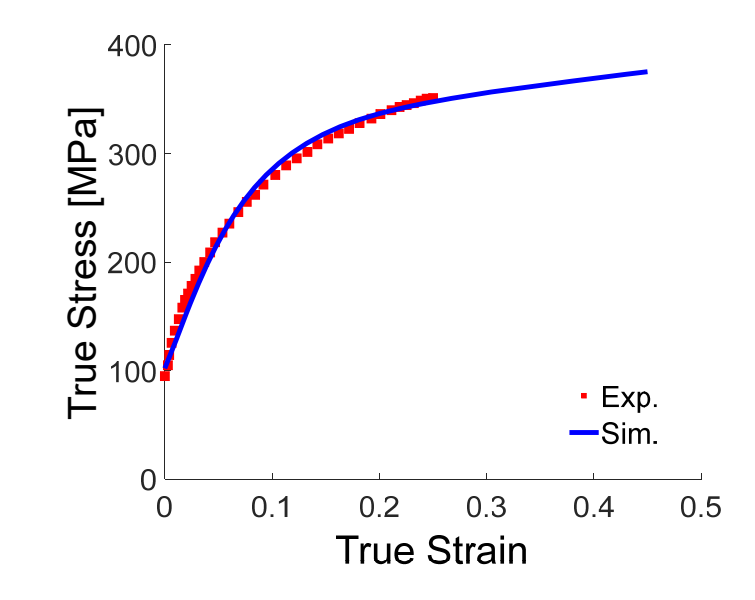


Figure D1. Comparison of experimentally measured (Exp.) and simulated (Sim) stress-strain curves for uniaxial tension along RD of AA5182-O.

Table D1. Hardening parameters for the evolution of slip resistance of AA5182-O alloy.

$\tau_{0,f}^{\alpha}$ [MPa]	$k_1^{\alpha} [m^{-1}]$	g^{α}	D^{α} [MPa]	q	$ ho_{0,for}^{lpha}$	$ ho_{0,sub}^{lpha}$	<i>b</i> ^α [m]	μ ^α [MPa]
28	1.16 ×10 ⁸	0.016	300	2	1×10^{12}	1 × 10 ⁻¹	2.56×10^{-10}	4.8 × 10 ⁴

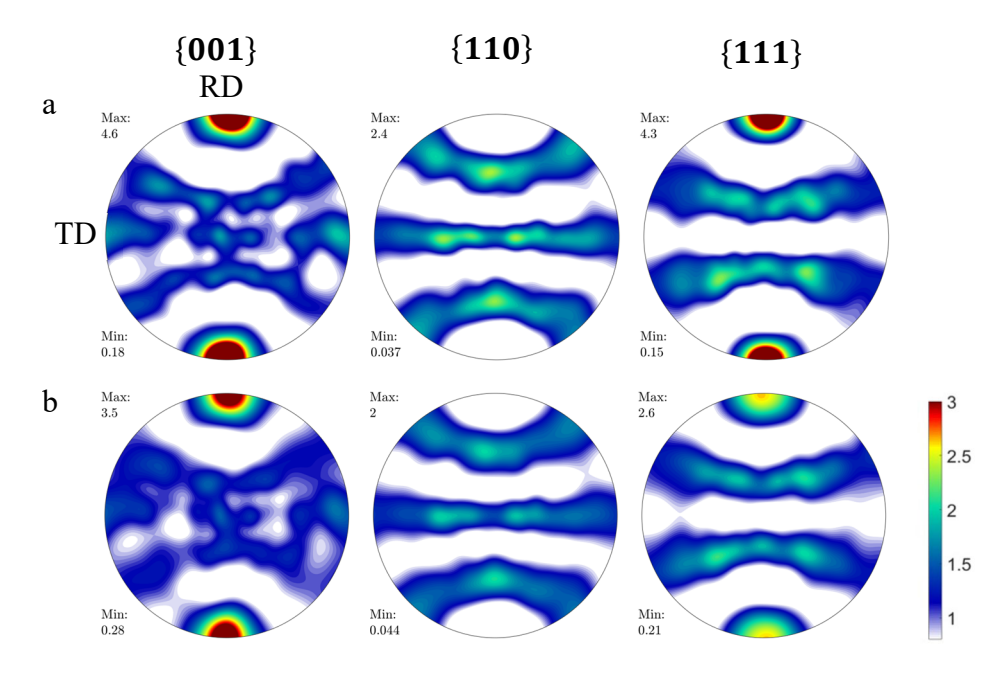


Figure D2. Pole figures of AA5182-O alloy: (a) predicted texture in tension along RD to a true strain of 0.45 after proper modeling of hardening and (b) predicted texture after tension followed by recrystallization.

References

- [1] A. Molinari, G.R. Canova, S. Ahzi. A self consistent approach of the large deformation polycrystal viscoplasticity, Acta Metallurgica 35 (1987) 2983-2994.
- [2] R.A. Lebensohn, C.N. Tomé. A self-consistent anisotropic approach for the simulation of plastic deformation and texture development of polycrystals: Application to zirconium alloys, Acta Metall. Mater. 41 (1993) 2611-2624.
- [3] M. Knezevic, R.J. McCabe, R.A. Lebensohn, C.N. Tomé, C. Liu, M.L. Lovato, B. Mihaila. Integration of self-consistent polycrystal plasticity with dislocation density based hardening laws within an implicit finite element framework: Application to low-symmetry metals, J. Mech. Phys. Solids 61 (2013) 2034-2046.
- [4] M. Zecevic, M. Knezevic, I.J. Beyerlein, R.J. McCabe. Texture formation in orthorhombic alpha-uranium under simple compression and rolling to high strains, Journal of Nuclear Materials 473 (2016) 143-156.

- [5] R. Masson, M. Bornert, P. Suquet, A. Zaoui. An affine formulation for the prediction of the effective properties of nonlinear composites and polycrystals, Journal of the Mechanics and Physics of Solids 48 (2000) 1203-1227.
- [6] M. Zecevic, R.A. Lebensohn, M. Rogers, J. Moore, V. Chiravalle, E. Lieberman, D. Dunning, G. Shipman, M. Knezevic, N. Morgan. Viscoplastic self-consistent formulation as generalized material model for solid mechanics applications, Applications in Engineering Science 6 (2021) 100040.
- [7] I.J. Beyerlein, M. Knezevic. Review of microstructure and micromechanism-based constitutive modeling of polycrystals with a low-symmetry crystal structure, Journal of Materials Research 33 (2018) 3711-3738.
- [8] R.A. Lebensohn, A.K. Kanjarla, P. Eisenlohr. An elasto-viscoplastic formulation based on fast Fourier transforms for the prediction of micromechanical fields in polycrystalline materials, Int. J. Plast. 32-33 (2012) 59-69.
- [9] M. Knezevic, B. Drach, M. Ardeljan, I.J. Beyerlein. Three dimensional predictions of grain scale plasticity and grain boundaries using crystal plasticity finite element models, Computer Methods in Applied Mechanics and Engineering 277 (2014) 239-259.
- [10] M. Knezevic, M. Jahedi, Y.P. Korkolis, I.J. Beyerlein. Material-based design of the extrusion of bimetallic tubes, Comput. Mater. Sci. 95 (2014) 63-73.
- [11] M. Zecevic, M. Knezevic, I.J. Beyerlein, R.J. McCabe. Origin of texture development in orthorhombic uranium, Mater. Sci. Eng. A 665 (2016) 108-124.
- [12] R.A. Lebensohn, Y. Liu, P. Ponte Castañeda. On the accuracy of the self-consistent approximation for polycrystals: comparison with full-field numerical simulations, Acta. Mater. 52 (2004) 5347-5361.
- [13] R.A. Lebensohn, C.N. Tomé, P.P. Castaneda. Self-consistent modelling of the mechanical behaviour of viscoplastic polycrystals incorporating intragranular field fluctuations, Philosophical Magazine 87 (2007) 4287-4322.
- [14] M. Ardeljan, M. Knezevic, T. Nizolek, I.J. Beyerlein, N.A. Mara, T.M. Pollock. A study of microstructure-driven strain localizations in two-phase polycrystalline HCP/BCC composites using a multi-scale model, Int. J. Plast. 74 (2015) 35-57.
- [15] M. Jahedi, I.J. Beyerlein, M.H. Paydar, M. Knezevic. Effect of Grain Shape on Texture Formation during Severe Plastic Deformation of Pure Copper Advanced Engineering Materials 20 (2018) 1600829.
- [16] M. Knezevic, H.F. Al-Harbi, S.R. Kalidindi. Crystal plasticity simulations using discrete Fourier transforms, Acta. Mater. 57 (2009) 1777-1784.
- [17] M. Knezevic, S.R. Kalidindi, D. Fullwood. Computationally efficient database and spectral interpolation for fully plastic Taylor-type crystal plasticity calculations of face-centered cubic polycrystals, Int. J. Plast. 24 (2008) 1264-1276.
- [18] M. Knezevic, T. Nizolek, M. Ardeljan, I.J. Beyerlein, N.A. Mara, T.M. Pollock. Texture evolution in two-phase Zr/Nb lamellar composites during accumulative roll bonding, International Journal of Plasticity 57 (2014) 16-28.
- [19] M. Knezevic, I.J. Beyerlein, M.L. Lovato, C.N. Tomé, A.W. Richards, R.J. McCabe. A strain-rate and temperature dependent constitutive model for BCC metals incorporating non-Schmid effects: Application to tantalum–tungsten alloys, Int. J. Plast. 62 (2014) 93-104.
- [20] M. Knezevic, I.J. Beyerlein, T. Nizolek, N.A. Mara, T.M. Pollock. Anomalous basal slip activity in zirconium under high-strain deformation, Mater. Res. Lett. 1 (2013) 133-140.

- [21] M. Knezevic, I.J. Beyerlein. Multiscale Modeling of Microstructure-Property Relationships of Polycrystalline Metals during Thermo-Mechanical Deformation, Advanced Engineering Materials 20 (2018) 1700956.
- [22] R.A. Lebensohn, Y. Liu, P.P. Castañeda. On the accuracy of the self-consistent approximation for polycrystals: comparison with full-field numerical simulations, Acta Materialia 52 (2004) 5347-5361.
- [23] P. Ponte Castañeda. Second-order homogenization estimates for nonlinear composites incorporating field fluctuations: I—theory, Journal of the Mechanics and Physics of Solids 50 (2002) 737-757.
- [24] P. Ponte Castañeda. Second-order homogenization estimates for nonlinear composites incorporating field fluctuations: II—applications, Journal of the Mechanics and Physics of Solids 50 (2002) 759-782.
- [25] Y. Liu, P. Ponte Castañeda. Second-order theory for the effective behavior and field fluctuations in viscoplastic polycrystals, Journal of the Mechanics and Physics of Solids 52 (2004) 467-495.
- [26] S. Das, P. Ponte Castañeda. Statistics of the stress, strain-rate and spin fields in viscoplastic polycrystals, International Journal of Solids and Structures 217-218 (2021) 193-214.
- [27] D. Song, P. Ponte Castañeda. Fully optimized second-order homogenization estimates for the macroscopic response and texture evolution of low-symmetry viscoplastic polycrystals, International Journal of Plasticity 110 (2018) 272-293.
- [28] R.A. Lebensohn, M. Zecevic, M. Knezevic, R.J. McCabe. Average intragranular misorientation trends in polycrystalline materials predicted by a viscoplastic self-consistent approach, Acta. Mater. 104 (2016) 228-236.
- [29] M. Zecevic, W. Pantleon, R.A. Lebensohn, R.J. McCabe, M. Knezevic. Predicting intragranular misorientation distributions in polycrystalline metals using the viscoplastic self-consistent formulation, Acta. Mater. 140 (2017) 398-410.
- [30] M. Zecevic, R.A. Lebensohn, R.J. McCabe, M. Knezevic. Modeling of intragranular misorientation and grain fragmentation in polycrystalline materials using the viscoplastic self-consistent formulation, Int. J. Plast. 109 (2018) 193-211.
- [31] M. Zecevic, R.A. Lebensohn, R.J. McCabe, M. Knezevic. Modelling recrystallization textures driven by intragranular fluctuations implemented in the viscoplastic self-consistent formulation, Acta. Mater. 164 (2019) 530-546.
- [32] R.D. Doherty. The Deformed State and Nucleation of Recrystallization, Metal Science 8 (1974) 132-142.
- [33] I.L. Dillamore, H. Katoh. The Mechanisms of Recrystallization in Cubic Metals with Particular Reference to Their Orientation-Dependence, Metal Science 8 (1974) 73-83.
- [34] R.D. Doherty, D.A. Hughes, F.J. Humphreys, J.J. Jonas, D.J. Jensen, M.E. Kassner, W.E. King, T.R. McNelley, H.J. McQueen, A.D. Rollett. Current issues in recrystallization: a review, Mater. Sci. Eng. A 238 (1997) 219-274.
- [35] H.R. Wenk, G. Canova, Y. Bréchet, L. Flandin. A deformation-based model for recrystallization of anisotropic materials, Acta Materialia 45 (1997) 3283-3296.
- [36] L.S. Tóth, Y. Estrin, R. Lapovok, C. Gu. A model of grain fragmentation based on lattice curvature, Acta Materialia 58 (2010) 1782-1794.
- [37] G.C. Butler, D.L. McDowell. Polycrystal constraint and grain subdivision, Int. J. Plast. 14 (1998) 703-717.

- [38] R. Lebensohn, H.-R. Wenk, C. Tomé. Modelling deformation and recrystallization textures in calcite, Acta Materialia 46 (1998) 2683-2693.
- [39] H.-R. Wenk, C.N. Tomé. Modeling dynamic recrystallization of olivine aggregates deformed in simple shear, Journal of Geophysical Research 104 (1999) 25,513-525,527.
- [40] F. Humphreys, M. Hatherly. Recrystallization and related annealing phenomena, 2004. Elsevier, 2004.
- [41] P.A. Beck, P.R. Sperry. Strain induced grain boundary migration in high purity aluminum, Journal of applied physics 21 (1950) 150-152.
- [42] I. Dillamore, P. Morris, C. Smith, W. Hutchinson. Transition bands and recrystallization in metals, Proc. R. Soc. Lond. A 329 (1972) 405-420.
- [43] A. Ridha, W. Hutchinson. Recrystallisation mechanisms and the origin of cube texture in copper, Acta metallurgica 30 (1982) 1929-1939.
- [44] J. Hjelen, R. Orsund, E. Nes. On the origin of recrystallization textures in aluminium, Acta Metall. Mater. 39 (1991) 1377-1404.
- [45] H. Bunge, U. Köhler. Model calculations of primary recrystallization textures, Scripta metallurgica et materialia 27 (1992) 1539-1543.
- [46] O. Engler. A simulation of recrystallization textures of Al-alloys with consideration of the probabilities of nucleation and growth, Texture, Stress, and Microstructure 32 (1999) 197-219.
- [47] J. Park, M. Rout, K.-M. Min, S.-F. Chen, M.-G. Lee. A fully coupled crystal plasticity-cellular automata model for predicting thermomechanical response with dynamic recrystallization in AISI 304LN stainless steel, Mechanics of Materials 167 (2022) 104248.
- [48] J. Hirsch, K. Lucke. Mechanism of deformation and development of rolling textures in polycrystalline FCC metals I. Description of rolling texture development in homogeneous CuZn alloys, Acta Metall. Mater. 36 (1988) 2863-2882.
- [49] T. Leffers, R.K. Ray. The brass-type texture and its deviation from the copper-type texture, Prog. Mater. Sci. 54 (2009) 351-396.
- [50] H.F. Al-Harbi, M. Knezevic, S.R. Kalidindi. Spectral approaches for the fast computation of yield surfaces and first-order plastic property closures for polycrystalline materials with cubic-triclinic textures, CMC: Computers, Materials, & Continua 15 (2010) 153-172.
- [51] R. Smallman, D. Green. The dependence of rolling texture on stacking fault energy, Acta Metall. 12 (1964) 145-154.
- [52] I. Dillamore, W. Roberts. Rolling textures in fcc and bcc metals, Acta Metall. 12 (1964) 281-293.
- [53] M. Ardeljan, D.J. Savage, A. Kumar, I.J. Beyerlein, M. Knezevic. The plasticity of highly oriented nano-layered Zr/Nb composites, Acta. Mater. 115 (2016) 189-203.
- [54] M. Knezevic, S.R. Kalidindi. Crystal Plasticity Modeling of Microstructure Evolution and Mechanical Fields During Processing of Metals Using Spectral Databases, JOM 69 (2017) 830–838.
- [55] T. Leffers. The brass-type texture—how close are we to understand it? Materials Science Forum, vol. 702: Trans Tech Publ, 2012. p.216-223.
- [56] R.S. Kalidindi. Modeling anisotropic strain hardening and deformation textures in low stacking fault energy fcc metals, Int. J. Plast. 17 (2001) 837-860.
- [57] c.S. Lee, B.J. Duggan. Modified theory of rolling texture development in α brass, Materials Science and Technology 10 (1994) 155-161.

- [58] S.R. Kalidindi. Incorporation of deformation twinning in crystal plasticity models, Journal of the Mechanics and Physics of Solids 46 (1998) 267-290.
- [59] T. Leffers, D.J. Jensen. The Early Stages of the Development of Rolling Texture in Copper and Brass, Textures and Microstructures 8 (1988) 451034.
- [60] R. Lebensohn, T. Leffers. The rules for the lattice rotation accompanying slip as derived from a self-consistent model, Textures and microstructures 31 (1999) 217-230.
- [61] M. Ardeljan, M. Knezevic. Explicit modeling of double twinning in AZ31 using crystal plasticity finite elements for predicting the mechanical fields for twin variant selection and fracture analyses, Acta. Mater. 157 (2018) 339-354.
- [62] T. Leffers. A modified Sachs approach to the plastic deformation of polycrystals as a realistic alternative to the Taylor model. Strength of metals and alloys. Elsevier, 1979. pp. 769-774.
- [63] W. Wen, S. M'Guil, S. Ahzi, J.J. Gracio. Coupled effects of the lattice rotation definition, twinning and interaction strength on the FCC rolling texture evolution using the viscoplastic φ-model, International Journal of Plasticity 46 (2013) 23-36.
- [64] M. Wroński, K. Wierzbanowski, T. Leffers. On the lattice rotations accompanying slip, Materials Science and Technology 29 (2013) 129-133.
- [65] M. Miraglia, P. Dawson, T. Leffers. On the influence of mechanical environment on the emergence of brass textures in FCC metals, Acta. Mater. 55 (2007) 799-812.
- [66] A. Després, M. Zecevic, R.A. Lebensohn, J.D. Mithieux, F. Chassagne, C.W. Sinclair. Contribution of intragranular misorientations to the cold rolling textures of ferritic stainless steels, Acta Materialia 182 (2020) 184-196.
- [67] R. Quey, P.R. Dawson, J.H. Driver. Grain orientation fragmentation in hot-deformed aluminium: Experiment and simulation, Journal of the Mechanics and Physics of Solids 60 (2012) 509-524.
- [68] M. Jahedi, M. Ardeljan, I.J. Beyerlein, M.H. Paydar, M. Knezevic. Enhancement of orientation gradients during simple shear deformation by application of simple compression, J. Appl. Phys. 117 (2015) 214309.
- [69] M. Zecevic, M. Knezevic. A new visco-plastic self-consistent formulation implicit in dislocation-based hardening within implicit finite elements: Application to high strain rate and impact deformation of tantalum, Computer Methods in Applied Mechanics and Engineering 341 (2018) 888-916.
- [70] P. Lequeu, P. Gilormini, F. Montheillet, B. Bacroix, J.J. Jonas. Yield Surfaces for Textured Polycrystals .1. Crystallographic Approach, Acta Metallurgica 35 (1987) 439-451.
- [71] P. Van Houtte. Simulation of the rolling and shear texture of brass by the Taylor theory adapted for mechanical twinning, Acta Metall. Mater. 26 (1978) 591-604.
- [72] W.G. Feather, S. Ghorbanpour, D.J. Savage, M. Ardeljan, M. Jahedi, B.A. McWilliams, N. Gupta, C. Xiang, S.C. Vogel, M. Knezevic. Mechanical response, twinning, and texture evolution of WE43 magnesium-rare earth alloy as a function of strain rate: Experiments and multi-level crystal plasticity modeling, Int. J. Plast. 120 (2019) 180-204.
- [73] W.G. Feather, D.J. Savage, M. Knezevic. A crystal plasticity finite element model embedding strain-rate sensitivities inherent to deformation mechanisms: Application to alloy AZ31, Int. J. Plast. 143 (2021) 103031.
- [74] M. Knezevic, M. Zecevic, I.J. Beyerlein, R.A. Lebensohn. A numerical procedure enabling accurate descriptions of strain rate-sensitive flow of polycrystals within crystal visco-

- plasticity theory, Computer Methods in Applied Mechanics and Engineering 308 (2016) 468-482.
- [75] M. Zecevic, I.J. Beyerlein, R.J. McCabe, B.A. McWilliams, M. Knezevic. Transitioning rate sensitivities across multiple length scales: Microstructure-property relationships in the Taylor cylinder impact test on zirconium, Int. J. Plast. 84 (2016) 138-159.
- [76] C.N. Tome, R.A. Lebensohn. Material Modeling with the Visco-Plastic Self-Consistent (VPSC) Approach: Theory and Practical Applications, Elsevier, 2023.
- [77] C.N. Tomé, R.A. Lebensohn. Manual for Code Viscoplastic Self-consistent (version 7c). (2011).
- [78] J.D. Eshelby. The determination of the elastic field of an ellipsoidal inclusion, and related problems, Proc R. Soc. Lond. A 241 (1957) 376-396.
- [79] M. Bobeth, G. Diener. Static elastic and thermoelastic field fluctuations in multiphase composites, Journal of the Mechanics and Physics of Solids 35 (1987) 137-149.
- [80] W. Pantleon. Retrieving orientation correlations in deformation structures from orientation maps, Materials Science and Technology 21 (2005) 1392-1396.
- [81] S. Krog-Pedersen, J. Bowen, W. Pantleon. Quantitative characterization of the orientation spread within individual grains in copper after tensile deformation, International Journal of Materials Research INT J MATER RES 100 (2009) 433-438.
- [82] I. Allen C. Miller, T.R. Rice. Discrete Approximations of Probability Distributions, Management Science 29 (1983) 352-362.
- [83] H. Vazquez-Leal, R. Castaneda-Sheissa, U. Filobello-Nino, A. Sarmiento-Reyes, J. Sanchez Orea. High Accurate Simple Approximation of Normal Distribution Integral, Mathematical Problems in Engineering 2012 (2012) 124029.
- [84] R. Doherty, D. Hughes, F. Humphreys, J. Jonas, D.J. Jensen, M. Kassner, W. King, T. McNelley, H. McQueen, A. Rollett. Current issues in recrystallization: a review, Materials Science and Engineering: A 238 (1997) 219-274.
- [85] O. Engler. Nucleation and growth during recrystallisation of aluminium alloys investigated by local texture analysis, Materials Science and Technology 12 (1996) 859-872.
- [86] D. Hull, D.J. Bacon. Introduction to dislocations, Butterworth-Heinemann, 2001.
- [87] J.P. Hirth, J. Lothe. Theory of dislocations, (1982).
- [88] R.J. McCabe, A.W. Richards, D.R. Coughlin, K.D. Clarke, I.J. Beyerlein, M. Knezevic. Microstructure effects on the recrystallization of low-symmetry alpha-uranium, Journal of Nuclear Materials 465 (2015) 189-195.
- [89] I. Dillamore, H. Katoh. Mechanisms of recrystallization in cubic metals with particular reference to their orientation-dependence., Metal Science 8 (1974) 73-83.
- [90] N. Hansen, D.J. Jensen. Development of microstructure in FCC metals during cold work, Philosophical Transactions of the Royal Society of London A: Mathematical, Physical and Engineering Sciences 357 (1999) 1447-1469.
- [91] F.J. Humphreys, M. Hatherly. Chapter 2 The Deformed State. in: Humphreys FJ, Hatherly M, (Eds.). Recrystallization and Related Annealing Phenomena (Second Edition). Elsevier, Oxford, 2004. pp. 11-II.
- [92] A. Eghtesad, M. Zecevic, R.A. Lebensohn, R.J. McCabe, M. Knezevic. Spectral database constitutive representation within a spectral micromechanical solver for computationally efficient polycrystal plasticity modelling, Comput. Mech. 61 (2018) 89-104.
- [93] A. Eghtesad, T.J. Barrett, K. Germaschewski, R.A. Lebensohn, R.J. McCabe, M. Knezevic. OpenMP and MPI implementations of an elasto-viscoplastic fast Fourier transform-

- based micromechanical solver for fast crystal plasticity modeling, Advances in Engineering Software 126 (2018) 46-60.
- [94] A. Eghtesad, K. Germaschewski, M. Knezevic. Coupling of a multi-GPU accelerated elasto-visco-plastic fast Fourier transform constitutive model with the implicit finite element method, Comput. Mater. Sci. 208 (2022) 111348.
- [95] A. Eghtesad, K. Germaschewski, R.A. Lebensohn, M. Knezevic. A multi-GPU implementation of a full-field crystal plasticity solver for efficient modeling of high-resolution microstructures, Computer Physics Communications 254 (2020) 107231.
- [96] A. Eghtesad, M. Knezevic. A new approach to fluid–structure interaction within graphics hardware accelerated smooth particle hydrodynamics considering heterogeneous particle size distribution, Computational Particle Mechanics 5 (2018) 387-409.
- [97] H. Hu, P.R. Sperry, P.A. Beck. Rolling Textures in Face-Centered Cubic Metals, JOM Journal of the Minerals, Metals and Materials Society 4 (1952) 76-81.
- [98] A. Uniwersał, M. Wrobel, K. Wierzbanowski, M. Wroński. Effect of Asymmetric Cold Rolling on Texture of a Commercially Pure Copper, Acta Physica Polonica A 130 (2016) 1049-1052.
- [99] R.E. Smallman, D. Green. The dependence of rolling texture on stacking fault energy, Acta Metallurgica 12 (1964) 145-154.
- [100] C. Donadille, R. Valle, P. Dervin, R. Penelle. Development of texture and microstructure during cold-rolling and annealing of F.C.C. alloys: Example of an austenitic stainless steel, Acta Metallurgica 37 (1989) 1547-1571.
- [101] J. Hirsch, K. Lücke. Overview no. 76: Mechanism of deformation and development of rolling textures in polycrystalline f.c.c. metals—I. Description of rolling texture development in homogeneous CuZn alloys, Acta Metallurgica 36 (1988) 2863-2882.
- [102] I.L. Dillamore. Factors affecting the rolling recrystallisation textures in F.C.C. metals, Acta Metallurgica 12 (1964) 1005-1014.
- [103] U. Schmidt, K. Lücke. Recrystallization Textures of Silver, Copper and α -Brasses With Different Zinc-Contents as a Function of the Rolling Temperature, Texture of Crystalline Solids 3 (1979) 146381.
- [104] D. Zhang, L. Jiang, B. Zheng, J.M. Schoenung, S. Mahajan, E. Lavernia, I.J. Beyerlein. Deformation Twinning (Update). 2016.
- [105] S.R. Kalidindi. Modeling the strain hardening response of low SFE FCC alloys, Int. J. Plast. 14 (1998) 1265-1277.
- [106] J. Ha, S. Mayer, Z. Feng, N. Matukhno, M. Knezevic, B.L. Kinsey. Inducing <111> texture in AA5182-O through continuous-bending-under-tension and recovery heat treatment processes to influence r-values, CIRP Annals (2022).
- [107] M. Zecevic, M. Knezevic. Modeling of Sheet Metal Forming Based on Implicit Embedding of the Elasto-Plastic Self-Consistent Formulation in Shell Elements: Application to Cup Drawing of AA6022-T4, JOM 69 (2017) 922-929.
- [108] M. Zecevic, M. Knezevic. Latent hardening within the elasto-plastic self-consistent polycrystal homogenization to enable the prediction of anisotropy of AA6022-T4 sheets, Int. J. Plast. 105 (2018) 141-163.
- [109] M. Zecevic, T. Roemer, M. Knezevic, Y. Korkolis, B. Kinsey. Residual Ductility and Microstructural Evolution in Continuous-Bending-under-Tension of AA-6022-T4, Materials 9 (2016) 130.

- [110] T.J. Roemer, T.J. Barrett, M. Knezevic, B.L. Kinsey, Y.P. Korkolis. Experimental study of continuous-bending-under-tension of AA6022-T4, Journal of Materials Processing Technology 266 (2019) 707-714.
- [111] T.J. Barrett, S. Takagi, N. Islam, T. Kuwabara, T. Hassan, B.L. Kinsey, M. Knezevic, Y.P. Korkolis. Material modeling and simulation of continuous-bending-under-tension of AA6022-T4, Journal of Materials Processing Technology 287 (2021) 116658.
- [112] T.J. Barrett, M. Knezevic. Modeling material behavior during continuous bending under tension for inferring the post-necking strain hardening response of ductile sheet metals: Application to DP 780 steel, International Journal of Mechanical Sciences 174 (2020) 105508.
- [113] C.M. Poulin, Y.P. Korkolis, B.L. Kinsey, M. Knezevic. Over five-times improved elongation-to-fracture of dual-phase 1180 steel by continuous-bending-under-tension, Mater. Des. 161 (2019) 95-105.
- [114] C.M. Poulin, T.J. Barrett, M. Knezevic. Inferring Post-Necking Strain Hardening Behavior of Sheets by a Combination of Continuous Bending Under Tension Testing and Finite Element Modeling, Experimental Mechanics 60 (2020) 459-473.
- [115] C.M. Poulin, S.C. Vogel, Y.P. Korkolis, B.L. Kinsey, M. Knezevic. Experimental studies into the role of cyclic bending during stretching of dual-phase steel sheets, International Journal of Material Forming 13 (2020) 393-408.
- [116] T.J. Barrett, M. Knezevic. Deep drawing simulations using the finite element method embedding a multi-level crystal plasticity constitutive law: Experimental verification and sensitivity analysis, Computer Methods in Applied Mechanics and Engineering 354 (2019) 245-270.
- [117] M. Zecevic, M. Knezevic. A dislocation density based elasto-plastic self-consistent model for the prediction of cyclic deformation: Application to Al6022-T4, Int. J. Plast. 72 (2015) 200-217.
- [118] M. Knezevic, C.M. Poulin, X. Zheng, S. Zheng, I.J. Beyerlein. Strengthening of alloy AA6022-T4 by continuous bending under tension, Mater. Sci. Eng. A 758 (2019) 47-55.
- [119] N. Matukhno, N. Kljestan, S.C. Vogel, M. Knezevic. Improvements in elongation and tradeoffs in strength and ductility of several Mg sheet alloys through cyclic bending under tension and annealing, International Journal of Material Forming 16 (2023) 52.
- [120] N. Matukhno, N. Kljestan, S.C. Vogel, M. Knezevic. Cyclic bending under tension of alloy AZ31 sheets: Influence on elongation-to-fracture and strength, Mater. Sci. Eng. A 857 (2022) 144127.
- [121] N. Matukhno, N. Kljestan, M. Knezevic. Enhancing elongation and trading off strength versus ductility of commercially pure titanium sheets using cyclic bending under tension and annealing, International Journal of Solids and Structures 276 (2023) 112324.
- [122] W.C. Liu, T. Zhai, J.G. Morris. Comparison of recrystallization and recrystallization textures in cold-rolled DC and CC AA 5182 aluminum alloys, Materials Science and Engineering: A 358 (2003) 84-93.
- [123] J. Lv, J.-H. Zheng, V.A. Yardley, Z. Shi, J. Lin. A Review of Microstructural Evolution and Modelling of Aluminium Alloys under Hot Forming Conditions, Metals 10 (2020) 1516.
- [124] R. Kaibyshev, S. Malopheyev. Mechanisms of Dynamic Recrystallization in Aluminum Alloys, Materials Science Forum 794-796 (2014) 784-789.
- [125] F.J. Humphreys, M. Hatherly. Chapter 7 Recrystallization of Single-Phase Alloys. in: Humphreys FJ, Hatherly M, (Eds.). Recrystallization and Related Annealing Phenomena (Second Edition). Elsevier, Oxford, 2004. pp. 215-IV.

- [126] M. Knezevic, A. Bhattacharyya. Characterization of microstructure in Nb rods processed by rolling: Effect of grooved rolling die geometry on texture uniformity, International Journal of Refractory Metals and Hard Materials 66 (2017) 44-51.
- [127] N.C. Ferreri, S. Ghorbanpour, S. Bhowmik, R. Lussier, J. Bicknell, B.M. Patterson, M. Knezevic. Effects of build orientation and heat treatment on the evolution of microstructure and mechanical properties of alloy Mar-M-509 fabricated via laser powder bed fusion, Int. J. Plast. 121 (2019) 116-133.
- [128] S. Ghorbanpour, J. Bicknell, M. Knezevic. Fatigue strength of additive manufactured Mar-M-509 superalloy, Mater. Sci. Eng. A 840 (2022) 142913.
- [129] A. Eghtesad, T.J. Barrett, M. Knezevic. Compact reconstruction of orientation distributions using generalized spherical harmonics to advance large-scale crystal plasticity modeling: Verification using cubic, hexagonal, and orthorhombic polycrystals, Acta. Mater. 155 (2018) 418-432.
- [130] T.J. Barrett, A. Eghtesad, R.J. McCabe, B. Clausen, D.W. Brown, S.C. Vogel, M. Knezevic. A generalized spherical harmonics-based procedure for the interpolation of partial datasets of orientation distributions to enable crystal mechanics-based simulations, Materialia 6 (2019) 100328.
- [131] R.E. Marki, K.A. Brindley, R.J. McCabe, M. Knezevic. Crystal mechanics-based thermoelastic constitutive modeling of orthorhombic uranium using generalized spherical harmonics and first-order bounding theories, Journal of Nuclear Materials 560 (2022) 153472.
- [132] M. Knezevic, N.W. Landry. Procedures for reducing large datasets of crystal orientations using generalized spherical harmonics, Mechanics of Materials 88 (2015) 73-86.
- [133] A. Eghtesad, M. Knezevic. Modeling cyclic plasticity of additively manufactured alloy Mar-M-509 using a high-performance spectral-based micromechanical model, Applications in Engineering Science 7 (2021) 100065.
- [134] Z. Feng, R. Pokharel, S.C. Vogel, R.A. Lebensohn, D. Pagan, E. Zepeda-Alarcon, B. Clausen, R. Martinez, G.T. Gray, M. Knezevic. Crystal plasticity modeling of strain-induced martensitic transformations to predict strain rate and temperature sensitive behavior of 304 L steels: Applications to tension, compression, torsion, and impact, Int. J. Plast. 156 (2022) 103367.
- [135] N.C. Ferreri, Z. Feng, D.J. Savage, D.W. Brown, B. Clausen, T.A. Sisneros, M. Knezevic. In-situ high-energy X-ray diffraction and crystal plasticity modeling to predict the evolution of texture, twinning, lattice strains and strength during loading and reloading of beryllium, Int. J. Plast. 150 (2022) 103217.
- [136] N.C. Ferreri, S.C. Vogel, M. Knezevic. Determining volume fractions of γ , γ' , γ'' , δ , and MC-carbide phases in Inconel 718 as a function of its processing history using an advanced neutron diffraction procedure, Mater. Sci. Eng. A 781 (2020) 139228.
- [137] N.C. Ferreri, R. Pokharel, V. Livescu, D.W. Brown, M. Knezevic, J.-S. Park, M.A. Torrez, G.T. Gray. Effects of heat treatment and build orientation on the evolution of ϵ and α' martensite and strength during compressive loading of additively manufactured 304L stainless steel, Acta. Mater. 195 (2020) 59-70.
- [138] N.C. Ferreri, D.J. Savage, M. Knezevic. Non-acid, alcohol-based electropolishing enables high-quality electron backscatter diffraction characterization of titanium and its alloys: Application to pure Ti and Ti-6Al-4V, Mater. Charact. 166 (2020) 110406.
- [139] T. Urabe, J.J. Jonas. Modeling texture change during the recrystallization of an IF steel, ISIJ international 34 (1994) 435-442.

- [140] R. Ray, J.J. Jonas, R. Hook. Cold rolling and annealing textures in low carbon and extra low carbon steels, International materials reviews 39 (1994) 129-172.
- [141] V. Randle, O. Engler. Introduction to Texture Analysis. Macrotexture, Microstructure & Orientation Mapping, Gordon and Breach Science Publishers, 2000.
- [142] U. Von Schlippenbach, F. Emren, K. Lücke. Investigation of the development of the cold rolling texture in deep drawing steels by ODF-analysis, Acta metallurgica 34 (1986) 1289-1301.
- [143] K. Lücke, M. Hölscher. Rolling and recrystallization textures of BCC steels, Texture, Stress, and Microstructure 14 (1991) 585-596.
- [144] F. Emren, U. Von Schlippenbach, K. Lücke. Investigation of the development of the recrystallization textures in deep drawing steels by ODF analysis, Acta Metallurgica 34 (1986) 2105-2117.
- [145] I. Samajdar, B. Verlinden, P. Van Houtte, D. Vanderschueren. γ-Fibre recrystallization texture in IF-steel: an investigation on the recrystallization mechanisms, Materials Science and Engineering: A 238 (1997) 343-350.
- [146] A. Bhattacharyya, M. Knezevic, M. Abouaf. Characterization of Crystallographic Texture and Intra-Grain Morphology in Cross-Rolled Tantalum, Metall. Mater. Trans. A 46 (2015) 1085-1096.
- [147] N. Rajmohan, Y. Hayakawa, J. Szpunar, J. Root. Neutron diffraction method for stored energy measurement in interstitial free steel, Acta Materialia 45 (1997) 2485-2494.
- [148] D.J. Savage, I.J. Beyerlein, N.A. Mara, S.C. Vogel, R.J. McCabe, M. Knezevic. Microstructure and texture evolution in Mg/Nb layered materials made by accumulative roll bonding, Int. J. Plast. 125 (2020) 1-26.
- [149] M. Ardeljan, I.J. Beyerlein, M. Knezevic. A dislocation density based crystal plasticity finite element model: Application to a two-phase polycrystalline HCP/BCC composites, J. Mech. Phys. Solids 66 (2014) 16-31.
- [150] W. Hutchinson. Recrystallisation textures in iron resulting from nucleation at grain boundaries, Acta Metallurgica 37 (1989) 1047-1056.
- [151] K. Veasna, Z. Feng, Q. Zhang, M. Knezevic. Machine learning-based multi-objective optimization for efficient identification of crystal plasticity model parameters, Computer Methods in Applied Mechanics and Engineering 403 (2023) 115740.
- [152] D.J. Savage, Z. Feng, M. Knezevic. Identification of crystal plasticity model parameters by multi-objective optimization integrating microstructural evolution and mechanical data, Computer Methods in Applied Mechanics and Engineering 379 (2021) 113747.
- [153] M. Zecevic, M. Knezevic, B. McWilliams, R.A. Lebensohn. Modeling of the thermomechanical response and texture evolution of WE43 Mg alloy in the dynamic recrystallization regime using a viscoplastic self-consistent formulation, Int. J. Plast. 130 (2020) 102705.
- [154] M. Knezevic, M. Zecevic, I.J. Beyerlein, J.F. Bingert, R.J. McCabe. Strain rate and temperature effects on the selection of primary and secondary slip and twinning systems in HCP Zr, Acta. Mater. 88 (2015) 55-73.
- [155] L. Capolungo, I.J. Beyerlein, C.N. Tomé. Slip-assisted twin growth in hexagonal close-packed metals, Scr. Mater. 60 (2009) 32-35.